

AD-A178 115

INVESTIGATION OF THE IMPACT PERFORMANCE OF VARIOUS  
GLASS AND CERAMIC SYSTEMS(U) CAMBRIDGE UNIV (ENGLAND)  
CAYENDISH LAB D TOMMSEN ET AL 27 JAN 87

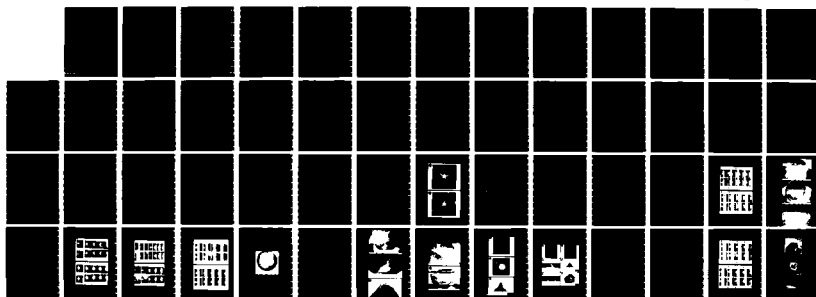
1/1

UNCLASSIFIED

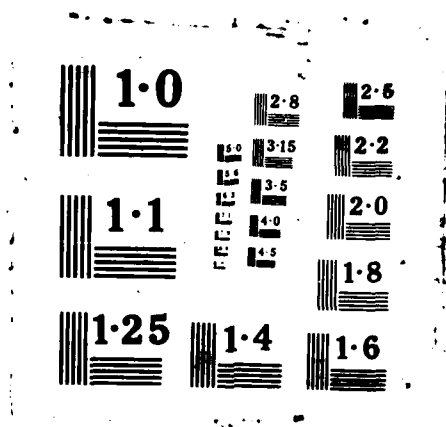
DAJ45-85-C-0021

F/8 11/2

NL



1 N/A  
4 1/2  
11/16



AD-A178 115

8

AD

**INVESTIGATION OF THE IMPACT PERFORMANCE  
OF VARIOUS GLASS AND CERAMIC SYSTEMS**

by

**Drs. D. Townsend & J.E. Field**

**January 1987**

**United States Army**

**EUROPEAN RESEARCH OFFICE OF THE U.S. ARMY**

**London, England**

**CONTRACT NUMBER DAJA45-85-C-0021**

**Cavendish Laboratory,  
Department of Physics,  
University of Cambridge,  
Madingley Road,  
Cambridge CB3 0HE, U.K.**

**DTIC  
ELECTE**

**MAR 16 1987**

**Approved for Public Release; distribution unlimited**

DTIC FILE COPY

UNCLASSIFIED

SECURITY CLASSIFICATION OF THIS PAGE

AD-178115

## REPORT DOCUMENTATION PAGE

Form Approved  
OMB No 0704 0188  
Exp Date Jun 30 1986

1a REPORT SECURITY CLASSIFICATION <b>UNCLASSIFIED</b>		1b RESTRICTIVE MARKINGS <b>NONE</b>							
2a SECURITY CLASSIFICATION AUTHORITY <b>USARDCG-UK</b>		3 DISTRIBUTION/AVAILABILITY OF REPORT  <b>UNLIMITED</b>							
2b DECLASSIFICATION/DOWNGRADING SCHEDULE <b>NOT APPLICABLE</b>									
4 PERFORMING ORGANIZATION REPORT NUMBER(S)		5 MONITORING ORGANIZATION REPORT NUMBER(S)  <b>ANNUAL</b>							
6a NAME OF PERFORMING ORGANIZATION <b>CAVENDISH LABORATORY</b>	6b OFFICE SYMBOL (If applicable)	7a NAME OF MONITORING ORGANIZATION <b>USARDCG-UK</b>							
6c ADDRESS (City, State, and ZIP Code) <b>MADINGLEY ROAD CAMBRIDGE UNIV. CAMBRIDGE, CB3 0HE, U.K.</b>		7b ADDRESS (City, State, and ZIP Code) <b>223 OLD MARYLEBONE RD. LONDON NW1 5TH, U.K.</b>							
8a NAME OF FUNDING SPONSORING ORGANIZATION <b>EUROPEAN RESEARCH OFFICE</b>	8b OFFICE SYMBOL (If applicable) <b>USARDCG-UK</b>	9 PROCUREMENT INSTRUMENT IDENTIFICATION NUMBER  <b>CONTRACT # DATA 45-85-C-0021</b>							
8c ADDRESS (City, State, and ZIP Code) <b>223 OLD MARYLEBONE RD. LONDON NW1 5TH, U.K.</b>		10 SOURCE OF FUNDING NUMBERS <table border="1"> <tr> <td>PROGRAM ELEMENT NO <b>61102A</b></td> <td>PROJECT NO <b>1161102BH57-04</b></td> <td>TASK NO</td> <td>WORK UNIT ACCESS ON NO</td> </tr> </table>		PROGRAM ELEMENT NO <b>61102A</b>	PROJECT NO <b>1161102BH57-04</b>	TASK NO	WORK UNIT ACCESS ON NO		
PROGRAM ELEMENT NO <b>61102A</b>	PROJECT NO <b>1161102BH57-04</b>	TASK NO	WORK UNIT ACCESS ON NO						
11 TITLE (Include Security Classification)  <b>"INVESTIGATION OF THE IMPACT PERFORMANCE OF VARIOUS GLASS AND CERAMIC SYSTEMS"</b>									
12 PERSONAL AUTHOR <b>DR. D. TOWNSEND AND DR. J. E. FIELD</b>									
13a TYPE OF REPORT <b>ANNUAL</b>	13b TIME COVERED FROM <b>JUL 85</b> TO <b>JUL 86</b>	14 DATE OF REPORT (Year, Month, Day) <b>JAN 27 1987</b>	15 PAGE COUNT <b>51 PAGES</b>						
16 SUPPLEMENTARY NOTATION  <b>NONE</b>									
17 COSAC CODES <table border="1"> <tr> <td>FIELD</td> <td>GROUP</td> <td>SUB-GROUP</td> </tr> <tr> <td></td> <td></td> <td></td> </tr> </table>		FIELD	GROUP	SUB-GROUP				18 SUBJECT TERMS (Continue on reverse if necessary and identify by block number) <b>Fracture, Impact, High-speed Photography, Hardness, Strength, Ceramics, Glasses</b>	
FIELD	GROUP	SUB-GROUP							
19 ABSTRACT (Continue on reverse if necessary and identify by block number) <p>This report describes a study of the strength impact and fracture behaviour of a range of ceramic materials. One part of the research is concerned with ceramics which have applications as radomes or infra-red transmitting window materials, the other with ceramics with potential application in body armour. Ceramics included in the study include zinc sulphide, various glass ceramics and aluminas, silicon carbide, silicon nitride, titanium diboride and boron carbide.</p> <p>In one series of experiments we have measured post-impact (i.e. residual) strength curves. These experiments involve impacting specimens at chosen velocities and then measuring the residual strengths after impact. Strength is plotted as a function of velocity. Such curves give: (i) the "threshold" velocity above which strength degradation following impact occurs; (ii) the fall in strength above the threshold; (iii) a ready comparison with other materials or between different batches of the same material which have had, for example, different surface preparations. From these strength curves, and a knowledge of <u>K<sub>1c</sub></u>, it is...</p>									
20 DISTRIBUTION/AVAILABILITY OF ABSTRACT <input type="checkbox"/> UNCLASSIFIED UNLIMITED <input type="checkbox"/> SAME AS RPT <input type="checkbox"/> DTIC USERS		21 ABSTRACT SECURITY CLASSIFICATION <b>UNCLASSIFIED</b>							
22a NAME OF RESPONSIBLE INDIVIDUAL <b>JORAL ALFARO CHIEF MATERIALS BRANCH</b>		22b TELEPHONE (Include Area Code) <b>400-1423</b>	22c OFFICE SYMBOL <b>FM</b>						

19. ABSTRACT (cont'd.)

*cont'd.* ...possible to estimate the size of the flaws which control the damage. Microscopy studies of the fracture faces have been made to locate the nucleating flaws so that there is a cross-check with the flaw sizes calculated.)

Gas guns have been used which can fire projectiles at velocities up to ca.  $800 \text{ m s}^{-1}$ . Higher velocities have been achieved using high-power rifles. High-speed photography, at microsecond framing rates, has been used extensively on this project to determine: (i) the modes of failure which depend markedly on the relative hardnesses of the projectile and target; (ii) the time sequence of failure; (iii) fracture velocities. The relationship between key mechanical properties and the performance of the ceramic in various applications is discussed.

In cases where physical property data were not available, they were measured. Tables give data on hardness, fracture toughness, elastic moduli, stress wave and fracture velocities.

*Keywords*

# INVESTIGATION OF THE IMPACT PERFORMANCE OF VARIOUS GLASS AND CERAMIC SYSTEMS

## TABLE OF CONTENTS

Page

### SUMMARY

1

### 1. LIQUID IMPACT TECHNIQUE

1

#### 1.1 Introduction

1

#### 1.2 The Water Jet Technique

2

#### 1.3 Impact Damage in Brittle Materials

2

#### 1.4 Impact Damage Assessment for Brittle Materials

2

#### 1.5 A Comparison of the Liquid Impact Performance of Various Brittle Materials

3

#### 1.6 Conclusions

4

### 2. SOLID PARTICLE IMPACT

4

#### 2.1 Introduction

4

#### 2.2 Apparatus

4

#### 2.3 Material Description

5

#### 2.4 Results and Discussion

7

##### 2.4.1 Glass Ceramic and Soda-lime Glass

7

##### 2.4.2 Alumina and Boron Carbide

8

#### 2.5 Conclusions

11

### REFERENCES

12

### TABLES

14

### FIGURE CAPTIONS

17

Accession For	
NTIS	<input checked="" type="checkbox"/>
DTIC	<input type="checkbox"/>
Unannounced	<input type="checkbox"/>
Justification	<input type="checkbox"/>
By _____	
Distribution _____	
Availability Codes	
Dist	Special
A-1	

## INVESTIGATION OF THE IMPACT PERFORMANCE OF VARIOUS GLASS AND CERAMIC SYSTEMS

This report describes our research to date on the impact behaviour of various glass and ceramic systems. It is divided into three sections. The first describes the liquid impact technique and the second covers experiments in which high velocity liquid jets were fired at specimens over a range of velocities and the "post impact" (i.e. "residual") strength measured. The jet technique is a convenient method for applying an intense stress pulse and studying the dynamic response of a material. If impact experiments are made over a range of velocities, it is possible to plot "residual" strength versus impact velocity. Such curves give the threshold velocity for damage and also show how rapidly the strength decreases for impacts above the threshold condition. Further, if the material  $K_{IC}$  is known, it is possible to calculate an "equivalent flaw" size. The residual strength curves obtained for the various materials are discussed.

The second section describes a study of the impact behaviour of glass and ceramic materials when impact by steel spheres. Velocities in the range up to  $900 \text{ m s}^{-1}$  were covered and the impact events recorded using high-speed photography at micro-second framing rates. There is no doubt that the response of materials to impact is complex with many factors involved. There is a great deal more which could be done (different projectile materials and shapes, laminated systems, effect of confinement, hard facings, etc.....). However, the research to date has made significant progress in identifying various failure modes and showing the importance of the target hardness compared to that of the projectile.

### 1 LIQUID IMPACT TECHNIQUE

#### 1.1 Introduction

The impact of a mass of liquid on a solid target comprises two distinct regimes of behaviour. Consider the impact of a cylindrical mass of liquid of radius  $r$  on a solid surface with velocity  $V$  (figure 1). The liquid initially behaves in a compressible manner (i.e. as a solid) until release waves, generated at the circumference of the jet, have reached the jet axis. The pressure,  $P$ , during this stage of the impact for a compressible target is given by

$$P = V \frac{p_1 c_1 p_2 c_2}{p_1 c_1 + p_2 c_2} \quad (1)$$

where  $p_1 c_1$  and  $p_2 c_2$  are the densities and shock wave velocities of the liquid and target material respectively. For a cylindrical jet of liquid the duration,  $\tau$ , of the compressible phase is given by

$$\tau = r / c \quad (2)$$

The initial high pressure stage is followed by incompressible flow of the liquid. The impact pressure drops to the Bernoulli stagnation pressure,  $P_B$ , given by

$$P_B = \rho V^2 / 2 \quad (3)$$

The pressure during this second stage of impact is very much lower, typically 10%, of the initial pressure. For this reason most of the impact damage in a brittle material is associated with the initial compressible phase.

## 1.2 The Water Jet Technique

The high velocity water jets are produced by a technique originally developed by Bowden and Brunton (1961) and subsequently modified by Field et al (1979b, 1983). The apparatus is illustrated in figure 2. A lead slug is fired from an air rifle into the rear of a water-filled stainless steel chamber. The forward motion of the sealing neoprene disc extrudes the water at high velocity through the orifice section at the front of the chamber. By careful design of the chamber, water jets with a coherent core of liquid can be produced. High-speed photographs of jets are illustrated in Field et al (1979b). The system is calibrated so that, by varying the firing pressure, a jet of a given velocity can be attained.

## 1.3 Impact Damage in Brittle Materials

Most of the damage in a brittle material is associated with the initial high pressure regime of the impact process. Dynamic loading of the solid during this stage generates compressive, shear, and Rayleigh surface waves (Bowden and Field 1964; Swain and Hagan 1980). Tensile components of the propagating surface wave cause extension of surface defects already present in the material during the loading time of the pulse (typically  $\leq 0.3 \mu\text{s}$ ). The resulting damage consists of an annulus of short circumferential cracks around the impact site (figure 3). The central area of the impact, corresponding approximately to the jet diameter, is undamaged by the compressive loading of the impact process. As the Rayleigh wave propagates, it initiates fracture at all the surface defects above a critical size. The short duration of the loading pulse,  $\leq 0.3 \mu\text{s}$ , means that the crack extension is limited. The liquid impact process can, therefore, be used to determine the distribution of surface defects in a material by examination of the impact damage produced.

## 1.4 Impact Damage Assessment for Brittle Materials

Optical examination of the impact damage is important but only provides qualitative information about the failure of the material. The impact damage in brittle materials can be assessed quantitatively by measuring the post-impact or residual strength.

Disc specimens of the material are impacted at the centre and the fracture stress measured using a hydraulic bursting technique (Gorham and Rickerby 1975; Matthewson and Field 1980). The apparatus is illustrated schematically in figure 4. A thin disc specimen is supported near its edge by a perfectly flat, hardened tool-steel ring. Hydrostatic pressure is transmitted from the oil to the rear of the specimen by a neoprene gasket. The pressure is increased until failure occurs. From the bursting pressure and position of the fracture origin, the fracture stress of the material can be calculated.

The main advantages of the hydraulic bursting technique compared with other strength measuring methods are:

- 1) Edge failures, which are caused by machining damage, are largely eliminated.
- 2) A large proportion of the specimen surface is tested.
- 3) The stress field is circularly symmetric with radial and tangential stresses of the same order of magnitude. The measured fracture stress is, therefore, virtually independent of the flaw orientation.
- 4) The ease and rapidity of operation.
- 5) The possibility of miniaturization; specimens down to 25 mm can be used.

The measured fracture stress,  $\sigma_f$ , and fracture toughness,  $K_{Ic}$ , can be used to calculate the size of the surface flaw,  $c$ , which caused the failure of the specimen in the strength test. In general, the equivalent flaw size can be calculated from the relation

$$c = \alpha [K_{Ic}/\sigma_f]^2 \quad (4)$$

where  $\alpha$  is a dimensionless constant depending on the flaw and stress field geometry.

Figure 5 shows a plot of fracture strength against impact velocity for soda-lime glass (van der Zwaag and Field 1983). The residual strength curve is typical of a brittle



material. A reduction in strength of the material is observed above a critical velocity. Liquid impacts below this threshold velocity do not produce sufficient stress to extend the surface defects. The surface flaw size distribution is not affected, therefore the post-impact strength is comparable to that for the unimpacted material. The threshold velocity is followed by a transition region in which the average fracture stress decays rapidly with increasing impact velocity. Field et al (1970a) observed a bimodal distribution of fracture stress in this region. Some specimens are undamaged by the impact, while others fail at a low stress due to extension of surface flaws. The variation in strength is attributed to the statistical nature of the flaw distribution in the specimen surface. A reduction in strength of the specimen will only be observed if there is a large enough surface defect present near the impact site to satisfy the conditions for crack growth. For high impact velocities, the average fracture stress is a much weaker function of impact velocity. All specimens show a loss in strength due to the impact. The increased pulse strength enables many more surface defects to propagate, but the short duration of the pulse limits their extension.

The residual strength curve is slightly modified for multiple jet impacts (van der Zwaag and Field 1983). The cracks are able to grow for each loading cycle of the impact providing the critical stress intensity is exceeded. An increase in the number of impacts therefore results in a decrease in the fracture stress of damaged specimens and a narrower transition region. The threshold velocity for impact damage is independent of the number of impacts. The accuracy in predicting the threshold velocity can be increased by using a multiple impact technique.

The residual strength technique provides accurate measurement of the threshold velocity for impact damage in brittle materials. The technique can also be used to assess changes in the impact performance of a material.

### 1.5 A Comparison of the Liquid Impact Performance of Various Brittle Materials

The residual strength curves for soda-lime glass, single crystal sapphire, polycrystalline alumina, and hot-pressed silicon nitride are shown in figure 6. Table 1 gives the threshold velocity for impact damage and the unimpacted fracture strength of these materials along with the fracture toughness, Vickers hardness, and inherent defect size.

The single crystal sapphire has the highest fracture strength of the materials tested due to the small inherent flaw size, ca. 10  $\mu\text{m}$ . The small surface defects contribute to the reasonably high threshold velocity,  $V_T$ , of  $300 \text{ m s}^{-1} < V_T < 350 \text{ m s}^{-1}$ . Above the threshold, the impact performance of this material is poor due to the low fracture toughness and high crack velocity, i.e. once fracture has initiated, the cracks extend considerably during the loading time of the impact pulse. Field (1962) observed that the maximum fracture velocity in single crystal sapphire is ca.  $4500 \text{ m s}^{-1}$ .

The polycrystalline alumina exhibited a low fracture strength,  $146 \pm 8 \text{ MPa}$ , which could be improved by a better surface preparation. The threshold velocity for alumina is similar to the value for single crystal sapphire, but the impact performance above the threshold is greatly improved. This can be attributed to the high toughness and low crack velocity of the alumina. Variability in porosity, grain size, and composition of alumina affects the fracture toughness and impact performance (Ferguson and Rice 1971; de With 1984). It is, therefore, important to control these parameters in the material used.

In spite of a small inherent flaw size (ca. 40  $\mu\text{m}$ ), soda-lime glass has a low fracture strength and low threshold velocity due to a low fracture toughness.

From the materials tested, the hot-pressed silicon nitride gave the best performance. A high initial strength and a very high threshold velocity were observed. Good impact performance above the threshold for damage arises from the high fracture toughness.

The impacts have been performed with water jets, but the equivalent threshold velocity,  $V$ , can be estimated for other projectiles from the expression

$$P = \frac{V \rho_w c_w}{\rho_w c_w + \rho_2 c_2} = \frac{V' \rho_s c_s}{\rho_s c_s + \rho_2 c_2} \quad (5)$$

where  $\rho_w c_w$ ,  $\rho_s c_s$  and  $\rho_2 c_2$  are the densities and shock wave velocities for water, the other projectile materials (for example, steel) and the target material respectively. For the impact of a mild steel cylindrical projectile, the equivalent threshold velocities are given in table 1. Equation 5 only holds if the pulse durations are of similar magnitude: this point will be discussed in more detail in later reports.

Hot-pressed silicon nitride has the highest predicted threshold velocity for impact damage by a mild steel projectile. The high hardness of this material will also contribute to give an excellent impact performance. The threshold velocity for alumina and sapphire are similar. Alumina will have the better performance due to its high toughness and low crack velocity. These calculations indicate that soda-lime glass will have the lowest threshold velocity for impact damage initiation by a mild steel solid particle. This results from the low fracture toughness and low modulus.

## 1.6 Conclusions

For the range of brittle materials included in this investigation, the jet technique and hydraulic strength test provide quantitative information on the threshold for damage and crack propagation during the loading pulse of the impact. The form of the residual strength curve can be related to the fracture toughness and crack velocity of the material. From the threshold velocity measurements the onset of impact damage by a solid particle can be predicted, thus providing a method of quantitatively ordering the materials with respect to damage initiation.

## 2 SOLID PARTICLE IMPACT

### 2.1 Introduction

The failure of various glass and ceramic materials when impacted by a hardened steel sphere is described in this section of the report. A small bore gas gun was used to accelerate the projectiles up to velocities of  $800 \text{ m s}^{-1}$ . These controlled impacts were photographed at microsecond framing rates with an image converter camera (Field, 1983). The fracture pattern of the impacted specimen and the damage to the projectile were recorded for each impact experiment. Results from these experiments have identified the various failure modes of the material during the impact process. The initial observations indicate that the hardness of the target and projectile are important parameters in determining the failure mechanism of the system.

### 2.2 Apparatus

The gas gun is shown schematically in figure 7. It consists of a cold drawn steel barrel, length 2 m and internal diameter 13.3 mm, connected by means of a breech to a pressure reservoir. The projectile, typically a hardened steel sphere 3 mm to 6 mm diameter, is mounted on the front face of a cylindrical, polyethylene sabot, length 25 mm. On firing, the sabot is accelerated down the barrel and then stopped by the muzzle block allowing the projectile to continue unimpeded. Reproducible impact velocities are obtained by using a double-diaphragm bursting technique (Hutchings and Winter, 1975). For a firing pressure  $P$ , diaphragms of a suitable material (e.g. copper foil) are chosen with a bursting pressure between  $P/2$  and  $P$ . The diaphragms are inserted into the breech as shown in figure 7. The reservoir and inter-diaphragm space are pressurised to  $P/2$  and then section B is isolated. Gas pressure in the reservoir is increased to  $P$ . Firing is achieved by venting the inter-diaphragm space to atmosphere. The pressure across the first diaphragm rises to  $P$  and it subsequently ruptures. Failure of the second diaphragm then occurs allowing the unimpeded gas flow to drive the sabot down the barrel. Using this technique, with gas pressures up to 4 MPa, projectile velocities in the range  $250 \text{ m s}^{-1}$  to  $800 \text{ m s}^{-1}$  can be achieved with

an accuracy of  $\pm 5\%$ . For lower velocities, the breech mechanism is replaced by a fast-acting solenoid valve. The range of velocities in this case is  $40 \text{ m s}^{-1}$  to  $400 \text{ m s}^{-1} \pm 3\%$ . The propellant gas can be either nitrogen or helium. Higher velocities are attained with helium due to its high acoustic wave velocity and low molecular weight (Seigel, 1965). Reducing the mass of the sabot by hollowing out the centre portion produces an increase in velocity of approximately 20%.

The impact velocity is determined from the time for the projectile to travel a measured distance in free flight. Two parallel light beams intersecting the path of the projectile define this distance (figure 8). The flash unit and image converter camera are triggered from the interruption of the second light beam. The triggering pulse is delayed to allow time for the projectile to reach the target before the camera and flash are activated. By placing the target close to the second light beam,  $< 20 \text{ mm}$ , small variations in velocity have a negligible effect on the delay time. With this experimental arrangement, more than 90% of the impact events are successfully recorded. For experiments involving a long flight path, a more complicated method for determining the delay time is necessary to ensure the same high success rate. In this case, the time of flight between the two beams is electronically processed while the projectile is in motion to give the delay time prior to impact (Pope, 1985). Care must be taken in both cases to ensure that the light level has reached full intensity before the camera is activated.

The specimen is supported along the upper and lower edges by two metal plates lined with neoprene rubber (figure 8). This method of support minimises the energy transmitted across the boundaries of the specimen by stress wave interaction.

The position of the camera and flash unit can be varied to record different views of the impact process under various lighting conditions.

### 2.3 Material description

The materials investigated in this report comprised polycrystalline alumina, glass ceramic, soda-lime glass and boron carbide. All the materials were in the form of tile specimens. The specimens were  $50 \text{ mm} \times 50 \text{ mm}$  with thicknesses in the range  $5 \text{ mm}$  to  $10 \text{ mm}$ . For each specimen, the impact was made at the centre of the square face.

A number of the mechanical properties of the materials under investigation have been measured. These properties include hardness ( $H$ ), fracture toughness ( $K_{Ic}$ ), longitudinal and shear wave velocities ( $C_l$ ,  $C_s$ ), bulk, shear and Young's moduli ( $K$ ,  $G$  and  $E$ ) and density ( $\rho$ ). A Vickers indenter was used to measure the hardness of each material. The hardness is defined as:

$$H = 1.854P/d^2 \quad (6)$$

where  $P$  is the indenter load and  $d$  the length of the diagonals of the plastic indent formed. The hardness values obtained for the materials are given in table 2.

The fracture toughness (critical stress intensity factor),  $K_{Ic}$ , was measured using the Vickers indentation technique (Lawn and Fuller, 1975). For this loading geometry,

$$K_{Ic} = \chi P/c^{3/2} \quad (7)$$

where  $P$  is the applied load,  $c$  the radius of the semi-circular median cracks produced by the indent and  $\chi$  a constant depending on indenter geometry and the coefficient of friction between indenter and sample. For this series of experiments  $\chi = 0.0726$ .  $K_{Ic}$  was evaluated from the gradient of the straight line plot of  $P$  versus  $c^{3/2}$  for each material. The fracture toughness values obtained are presented in table 4. Well-formed median cracks were not observed in boron carbide for indenter loads up to  $500 \text{ N}$ . The fracture toughness of this material cannot, therefore, be evaluated by the indentation technique.

The shear wave velocity and longitudinal wave velocity were determined from the transit time of shear and longitudinal stress pulses through a measured thickness

of the material. Figure 9a shows schematically the experimental configuration for measuring the shear wave velocity. An electrical pulse of typically 15 V and duration  $< 1 \mu\text{s}$  is applied to the transmitting transducer. Shear stresses at the receiver are converted to an electrical signal and then displayed on the storage oscilloscope. Figure 10a is a plot of the display obtained for shear wave velocity measurements in alumina. Channel 1 represents the voltage applied to the transmitter and channel 2 the voltage produced at the receiver; note the difference in scale of these signals. The shear wave velocity,  $C_s$ , in the material is given by:

$$C_s = d/t \quad (8)$$

where  $t$  is the transit time for the stress pulse and  $d$  is the appropriate dimension of the specimen. The values of  $C_s$  obtained for the materials investigated are given in table 3. A small disturbance,  $l$ , before the received shear wave pulse (figure 10a) is attributable to a longitudinal mode of vibration produced by the transducers and is, therefore, ignored. The complex waveform of the received pulse is due to 'ringing' of the transmitter and multiple stress wave reflections in the specimen. For these measurements this part of the waveform is disregarded.

The experimental configuration for measuring the longitudinal wave velocity,  $C_l$ , is shown schematically in figure 9b. Lead zirconate titanate longitudinal transducers are mounted on thin copper foil (0.03 mm) and then clamped at the centre of the faces of the specimens. A small quantity of petroleum jelly is placed between the components of the system to ensure good acoustic contact. Typically, an electrical pulse of  $< 10 \text{ V}$  and duration  $< 1 \mu\text{s}$  is applied across the transmitting transducer via the copper foil. Electrical signals generated by the longitudinal stress wave at the receiver are displayed on the oscilloscope. A plot of the display obtained for longitudinal stress wave measurements in a glass ceramic is shown in figure 10b. The voltage applied to the transmitter is represented as channel 1 and the output voltage from the receiver as channel 2; note the difference in scale of these signals. The time for the stress pulse to travel through the material,  $t$ , is measured from the rising edge of the loading pulse to the commencement of the received pulse. In practice, measurements of the stress wave velocity with one tile specimen are inaccurate because the trace on the oscilloscope represents the electrical signals at the transducers and not the stress waves in the material. This 'end error' problem is surmounted by measuring the time for the stress pulse to travel through a number of specimens and then subtracting the transit time observed for one specimen, e.g. 2 specimens of thicknesses  $d_1$  and  $d_2$  are shown in figure 9c. The total transit recorded for specimen 1 is  $t_1$  and the time for the stress pulse to pass through specimens 1 and 2 when in acoustic contact is  $t_2$ . Hence, the longitudinal stress wave velocity in specimen 2 is

$$C_2 = d_2 / (t_2 - t_1) \quad (9)$$

This procedure is repeated with three and four specimens in order to give a more accurate value of the longitudinal stress wave velocity in the material. In this instance, it is essential to have specimens with parallel faces to ensure good acoustic contact. The values of  $C_l$  obtained for the various materials are given in table 3. As in the case of the shear wave velocity measurements, the complex waveform observed at the receiver is due to 'ringing' of the transmitter and stress wave reflections in the material. For these experiments, this part of the waveform is ignored.

The shear wave and longitudinal wave velocities can be used to calculate the shear modulus, bulk modulus, Young's modulus and Poisson's ratio of the material. The shear transducer produces pure shear strains in the material (see, e.g. Blitz, 1967); therefore, the shear modulus,  $G$ , is given by

$$G = \rho C_s^2 \quad (10)$$

where  $\rho$  is the density of the material and  $C_s$  is the shear wave velocity. Table 3 gives the values of  $G$  and  $\rho$  for the materials investigated.

From elasticity theory (see e.g. Champion and Davy, 1961) for plane longitudinal waves with zero lateral strain the wave velocity  $C_l$  is given by:

$$C_l = \left( \frac{K + 4G/3}{\rho} \right)^{1/2} \quad (11)$$

where  $K$  is the bulk modulus of the material. In order to ensure that no lateral strain is generated in the material, the distance from the longitudinal transducer to the edges of the loading face must be greater than the wavelength of the stress wave. The longitudinal wave velocity is, therefore, measured through the thickness of the tile specimens (see Figure 9b). Rewriting equation 11 gives the bulk modulus  $K$ :

$$K = \rho C_l^2 - 4G/3 \quad (12)$$

## 2.4 Results and Discussion

### 2.4.1 Glass ceramic and soda-lime glass

The impact experiments were performed with a 5 mm diameter hardened steel sphere on tile specimens of thickness 9.8 mm at velocities in the range  $40 \text{ m s}^{-1}$  to  $900 \text{ m s}^{-1}$ . Figure 11 shows an example of a glass ceramic specimen after impact at  $240 \text{ m s}^{-1}$ . A schematic representation of the crack systems and the deformed zone formed in the glass ceramic over the range of velocities investigated is given in figure 12. Impact velocities of ca.  $40 \text{ m s}^{-1}$  generated a Hertzian-type ring crack on the surface of the specimen and a short cone crack in the material. Above  $55 \text{ m s}^{-1}$ , the cone cracks propagate to the rear of the glass ceramic specimen resulting in the expulsion of a cone of material. As the velocity of impact increases, the semi-apex angle of the cone produced decreases. A detailed discussion of the formation of the cone cracks and the variation of the semi-apex angle,  $\theta$ , with impact velocity will be given later.

The lateral crack system in the glass ceramic is evident at impact velocities greater than  $80 \text{ m s}^{-1}$ . Increasing the velocity of the impact increases the extent of the lateral cracking. Lateral cracks form during unloading of the material and grow from suitable defects at the elastic - plastic boundary of the deformed zone (Hagan and Swain, 1978). These cracks propagate under the action of the residual stresses caused by the mismatch at the boundary between the irreversible deformed material and the surrounding elastic matrix. They propagate in a saucer-like shape towards the surface of the material (figure 12). At high impact velocities ( $>200 \text{ m s}^{-1}$ ), the lateral cracks reach the surface of the glass ceramic specimen causing removal of material and thereby producing a "double cone" feature at the impact site. Higher impact velocities result in the removal of more material from the impact face by lateral crack growth. Traces where the lateral cracks reached the surface can be seen on the impact face of the specimen shown in figure 11.

Failure of the rear surface of an impacted glass ceramic specimen is caused by spalling combined with propagation of the cone crack and radial crack system.

The impact of the sphere on the target produces a compression wave in the material. Reflection of this wave at the rear surface of the specimen produces a tensile stress wave. At a sufficient stress level, the reflected tensile stress wave can initiate spall failure close to the rear face of the specimen (see, for example, Johnson, 1972). Spall failure is evident in the glass ceramic at velocities above ca.  $120 \text{ m s}^{-1}$ .

Radial cracks are caused by bending of the specimen during the impact loading and result in fragmentation of the tile. Impact velocities greater than  $60 \text{ m s}^{-1}$  cause radial cracking of the tile specimens. The number of radial cracks increases as the velocity of the impact increases due to the higher loads generated by the impact. In general the expelled cone of material, caused by the cone cracks reaching the rear surface of the specimen, contains radial fractures. These fractures align with the radial

fractures in the specimen, thus indicating that the radial cracks initiate from the rear surface of the specimen before the cone cracks have extended through the thickness of the tile (figure 13).

The semi-apex angle,  $\theta$ , of the cone crack produced by the impact was found to decrease as the impact velocity increased (figure 14). Measurement of the cone angle could not be made in specimens impacted above ca.  $400 \text{ m s}^{-1}$  due to the extensive damage arising from the impact. Knight et al. (1977) and Chaudhri (1985) have observed a similar trend of decreasing  $\theta$  with increasing velocity for impacts on "Pyrex" and fused silica glasses with steel balls. The variation of  $\theta$  with impact velocity is attributed to the expanding contact radius between the impacting projectile and the target. The typical stress trajectories for a Hertzian stress field are shown in figure 15 (Huber 1904, Lawn et al. 1974). These trajectories are such that the tangents and normals to the curves at any point indicate the directions of the principal stresses. The contact radius between the sphere and flat is represented by  $oa$ . For quasi-static indentations, a ring crack initiates from a suitable defect just outside the contact radius when sufficient stress has been generated in the specimen by the indentation load. Subsequent growth of the ring crack follows a stress trajectory thereby producing a cone crack.

During quasi-static indentation, if subsequent loading results in the contact area encompassing the surface traces of the cone crack, the cone crack ceases to propagate. In the case of a dynamic indentation, however, cone cracks within the area of contact continue to grow (Chaudhri et al, 1976, Knight et al, 1977). A cone crack which initiates during the impact loading at a point just outside the contact area will initially propagate along a stress trajectory near the point  $a$ . As the impact loading continues, the contact area expands therefore the cone crack will follow a stress trajectory which is in the region  $oa$ . From figure 15, it can be seen that these trajectories are at a steeper angle, the resulting cone crack will, therefore, have a smaller semi-apex angle compared with the quasi-static value.

For all impact velocities, the ring crack will initiate at approximately the same contact radius because the stresses generated in the substrate are principally dependent upon the contact area (Andrews, 1931; Adler, 1975). As the velocity of the impact increases the final contact area between the ball and the flat increases. The final stages of the cone crack propagation will, therefore, follow stress trajectories closer to  $o$  as the velocity of the impact increases. This results in a decrease in the semi-apex angle of the cone crack with increasing velocity as observed. Further work is needed to quantitatively analyse the variation of the cone angle with impact velocity.

Impacts on a small number of specimens produced cone cracks with an uncharacteristically small semi-apex angle (figure 14). The formation of these small angled cones is attributed to the presence of a large failure-initiating defect at the impact site. A ring crack will initiate from this defect at a low stress which corresponds to a small contact area. The later stages of cone crack propagation will, therefore, follow stress trajectories near the origin of the impact,  $o$ , resulting in a small angled cone.

For sufficiently high impact velocities, a second cone crack may form. This second cone failure initiates at a larger contact radius than the first cone and is consequently much shallower i.e. larger semi-apex angle. Woodward and Field (1974) have observed that for steel ball impacts on glass the second ring crack initiates before the first ring crack, from which the first cone crack propagates has been completed. Secondary cone cracks are observed in the glass ceramic for impact velocities above ca.  $300 \text{ m s}^{-1}$ . In general, measurements of the semi-apex angle of the secondary cone are difficult; however, a trend of decreasing cone angle with increasing impact velocity was observed. For very high impact velocities,  $>600 \text{ m s}^{-1}$ , multiple cone cracks of progressively shallower angles are observed.

Penetration of the 9.8 mm thick glass ceramic specimen by the projectile was achieved for impact velocities greater than  $450 \text{ m s}^{-1}$ . The mechanism and criterion for penetration is not clear at the present time. For penetration to occur, the loading time of the impact must be longer than the time for the cone crack to propagate through the specimen and secondly the residual energy of the projectile must be capable of



overcoming the frictional drag caused by abrasion with the crushed glass ceramic.

The hardened steel sphere on impact with the glass ceramic suffers a small degree of plastic deformation. It should be noted that the steel sphere is slightly harder than the glass ceramic. High-speed Imacon sequences (figure 16) of the impact show that a plume of fine high velocity particles, p, is produced from the contact area. This jetting of material results from deformation and crushing of the material beneath the sphere during impact. Scanning electron micrographs of the projectile (figure 17) after impact show areas, e, where the high velocity jetting material has eroded the projectile surface. Around this area is a region, g, in which the fine glass particles have remained embedded in the hardened steel sphere.

The central region of the projectile, u, is relatively undamaged. It is proposed that this central undamaged region corresponds to the initial contact area in which the contact velocity between the sphere and the target is greater than the velocity with which the crushed zone propagates through the material (figure 18). In this regime the fine particles generated in the crushed zone are essentially trapped beneath the sphere. As the contact velocity falls below the propagation velocity of the crushed zone, these particles can escape and form the jetting material shown in figure 16.

The propagation velocity of the crushed zone in transparent material can be estimated from high-speed photographs of the impact. Figures 19 and 20 show such sequences for soda-lime glass and a transparent glass ceramic. The sequences indicate that initially the crushed zone propagates at approximately  $1500 \text{ m s}^{-1}$  and  $2200 \text{ m s}^{-1}$  for soda-lime glass and the glass ceramic respectively. These velocities are equivalent to the terminal crack velocity in the materials.

The high-speed sequences shown in figures 19 and 20 have been used to estimate the crack velocity in the materials and to observe the formation of the crack systems. The impact velocity of the steel ball is  $250 \text{ m s}^{-1}$ . The crack velocity was estimated from the propagation of the cracks, c. These were chosen because they appear to be singly developing cracks, rather than fracture paths made up from multiply-nucleated cracks. The cracks are clearly near their limiting (maximum) velocity since there is evidence of crack branching. For the glass ceramic the maximum crack velocity is  $2300 \pm 100 \text{ m s}^{-1}$  and for soda-lime glass,  $1480 \pm 50 \text{ m s}^{-1}$ . The value observed for soda-lime glass is in good agreement with the values obtained by Field (1971),  $1580 \text{ m s}^{-1}$ , and Chaudhri et al (1976),  $1400 - 1500 \text{ m s}^{-1}$ .

Surface defects in the material, r, are extended by the Rayleigh surface wave generated by the impact (Bowden and Field 1964). In figure 19b it can be seen that the reflection of the stress wave from the upper and lower edges of the specimen produces a change in the direction of the propagating surface defects (frames 4 to 8). For this impact configuration, reflection of the loading pulse from the rear surface of the specimen (i.e. right-hand side of picture) did not significantly influence the crack propagation, though a small effect on the crack paths can be detected.

High-speed sequences,  $0.95 \mu\text{s}$  interframe time, of the impact process on thinner specimens are shown in figure 20. Figure 20a shows a 3mm diameter hardened steel sphere impact on a glass ceramic. Reflection of the compressive loading pulse as a tensile stress wave at the rear surface of the specimen causes the surface cracks, s. Lateral cracks, l, develop in frames 10 to 14 and reach the surface, resulting in the eventual removal of material from the impact face of the specimen. Similar crack patterns are observed in the soda-lime glass specimen shown in figure 30b.

#### 2.4.2 Alumina and Boron Carbide

Impacts were performed on 2" x 2" tile specimens, thickness 6mm to 11mm, of alumina and boron carbide. High-speed Imacon sequences of the impact of a 5mm diameter hardened steel sphere on alumina are shown in figure 21. For impact velocities up to approximately  $180 \text{ m s}^{-1}$ , the sphere rebounds from the surface of the material. High impact pressures generated, due to the high hardness of the alumina, result in extensive plastic deformation of the projectile and formation of a flat, F. As the impact velocity is increased, fracture of the projectile occurs. Figure 22 shows a scanning electron micrograph of a hardened steel sphere after impact at  $200 \text{ m s}^{-1}$  on

an alumina specimen. The cracks, C, are clearly visible along with the flat, F, caused by plastic deformation on impact. Increasing the velocity of impact produced more extensive deformation and fragmentation of the steel sphere. A schematic representation of the failure observed in the projectile is shown in figure 23. An "inverted cone", n, is formed in the projectile, the base area of this cone corresponding to the initial contact area between the sphere and the specimen. For sufficiently high impact loads, fracture planes, r, form in the sphere resulting in fragmentation. Scanning electron micrographs of the sphere fragments are shown in figure 24. This figure shows the flat formed, f, the fracture plane in the sphere, c, the flow lines, l, caused by extensive deformation of the material, and the cone of material, n, produced from the contact area. At sufficiently high impact velocities ( $> 400 \text{ m s}^{-1}$ ) the fragments of the projectile flow radially outwards across the surface of the tile producing a metallic deposit on the specimen. Figure 25 shows a hardened steel ball after impact at  $460 \text{ m s}^{-1}$  on an alumina specimen. The sphere has undergone extensive plastic deformation and the base of the "inverted cone" formed at the contact area, n, is shown along with the radial flow of material, q. At progressively higher impact velocities, the extent of deformation and fracture in the projectile increases. For all impact velocities, however, a cone of material formed during the initial contact is observed. Similar failure features have been observed for the fracture of brittle spheres on impact (Arbiter et al 1969; Tilly and Sage 1970).

The impact of a hardened steel sphere on an alumina tile specimen produces a Hertzian-type cone failure over the range of impact velocities investigated ( $50 \text{ m s}^{-1}$  -  $900 \text{ m s}^{-1}$ ). For impact velocities greater than ca.  $200 \text{ m s}^{-1}$  the cone crack propagates through the thickness of the specimen resulting in a cone of material as shown in figures 26 and 27. The cone of material consists of an upper smooth area and a lower roughened region. This roughened region is caused by the interaction of the propagating cone crack with the reflected tensile wave from the rear face of the specimen. In figure 27 the cone has fractured along the initial line of interaction. The reflected tensile wave also produces a change in the cone angle during the later stages of cone crack propagation. Figure 28 is a schematic representation of the cone crack formed in the alumina by the impact. The initial point of contact is represented by p and the image source of the reflected tensile pulse by the point p'. The point of interaction between the reflected tensile wave and the cone crack is shown at the position Y. Before the interaction, the tensile stress at the crack tip will be normal to the growing fracture, i.e. a a'. The tensile wave will effectively superimpose a stress b b' to give a resultant R R' which will cause the cone crack to change direction because tensile fracture propagates normal to the maximum tension at the crack tip. At sufficiently high impact velocities,  $> 500 \text{ m s}^{-1}$ , radial failure is observed in the cone of material following the radial crack trajectories present in the tile specimen.

Measurements of the semi-apex cone crack angle in the alumina specimens indicate that the semi-apex angle increases with increasing impact velocity (figure 29). This behaviour is the converse of the trend observed with the glass ceramic! For a hardened steel projectile impact on the glass ceramic, the expanding contact area between the projectile and specimen qualitatively accounted for the decrease of  $\theta$  with impact velocity. In the case of alumina, however, the projectile fractures on impact and thus limits the expansion of the contact area. Further, the radial flow of the projectile over the tile surface will generate shear stresses which may influence cone crack propagation. The cone crack initiates from a defect in the specimen surface, therefore the distribution of surface defects will influence the initiation point of the cone crack and thereby the cone angle (see figure 15).

High-speed Imacon sequences of the impact of a hardened steel sphere on an alumina specimen (figures 21 and 30) show that the high velocity plume of fine particles, evident with the glass ceramic, is not present. This indicates that the extent of deformation and/or crushing in the alumina is small. The alumina is harder than the steel projectile (table 2). In addition, lateral cracks are not observed in the alumina. The lateral crack system propagates under the action of residual stresses, caused by permanent deformation in the material, during the unloading cycle. Deformation of alumina during impact is minimal; consequently, the residual stresses are not sufficient



to nucleate and propagate the lateral crack system.

The failure produced by a hardened steel sphere impact on boron carbide is similar to that observed for impacts on alumina. A high-speed Imacon sequence of the impact of a steel sphere at a velocity of  $255 \text{ m s}^{-1}$  on boron carbide is shown in figure 30b. High impact pressures are generated due to the high hardness of the boron carbide resulting in failure of the projectile. The failure observed in the projectile is similar to that found for impacts on alumina. Figure 31 shows a boron carbide specimen after impact. The damage observed in the material is considerably greater than that produced in the alumina specimens due to the higher impact stresses. Impacts on boron carbide produce extensive radial cracking and a large area of failure on the rear of the specimen.

## 2.5 Conclusions

The experiments described in this report have identified the failure modes of the target material and projectile for a range of impact velocities and material parameters. The failure produced is dependent upon the relative hardness of the target and projectile. Materials with a hardness less than that of the projectile produce limited plastic deformation of the sphere. For sufficiently high impact velocities, penetration of the target by the projectile can be achieved. The impact of the steel sphere upon a harder specimen causes extensive deformation and fracture of the projectile; penetration of the target by the projectile is not observed.

From the materials investigated alumina and boron carbide offer the best impact resistance in the absence of a confining plate on the rear surface of the specimen. The performance of the materials will be dramatically affected by applying a backing plate to the rear surface of the specimen. This will restrain material and thus increase the resistance to penetration. An investigation of the impact performance of a composite armour comprising of an outer hard layer, e.g. boron carbide or alumina, an intermediate layer of a softer, e.g. glass ceramic or soda-lime glass and a backing plate of a fibre composite is to be undertaken. It is proposed that the outer hard layer will produce severe damage to the projectile while extensive fragmentation of the intermediate layer will increase the area of loading on the rear backing plate. The results of these experiments and crack velocity measurements will be described in subsequent reports.

## REFERENCES

- Adler W.F. - (1975) *J. Non-cryst. Solids* **19**, p.335.
- Andrews J.P. - (1930) *Lond. Edinb. Dubl. Phil. Mag.* **9**, p.593.
- Andrews J.P. - (1931) *Proc. Phys. Soc. Lond.* **43**, p.18.
- Arbiter N., Harris C.C. & Stamboltzis G.A. - (1969) *Trans. AIME* **244**, p.118.
- Blitz J. - (1967) *Fundamentals of Ultrasonics*, publ. Butterworth and Co., London.
- Bowden F.P. & Brunton J.H. - (1961) *Proc. Roy. Soc.* **A262**, p.433.
- Bowden F.P. & Field J.E. - (1964) *Proc. Roy. Soc.* **A282**, p.331.
- Champion F.C. & Davy N. - (1961) *Properties of Matter*, 3rd edn., publ. Blackie and Son Ltd., London.
- Chaudhri M.M. - (1985) in *Strength of "Inorganic Glass"*, NATO Conference Series VI : Materials Science, Plenum Press.
- Chaudhri M.M., Knight C.G. & Swain M.V. - (1976) *Proc. 12th Int. Cong. on High-Speed Photography*, Toronto, p.371.
- Dorre E. & Hubner M. - (1984) *Alumina Materials Research and Engineering*, publ. Springer-Verlag, Berlin.
- Ferguson W.J. & Rice R.W. - (1971) *Mat. Sci. Research* **5**, p.261.
- Field J.E. - (1962) Ph.D Thesis, University of Cambridge.
- Field J.E. - (1971) *Contemp. Phys.* **12**, No. 1, p.1.
- Field J.E. - (1983) *Contemp. Phys.* **24**, No. 5, p.439-459.
- Field J.E., Camus J.J. & Gorham D.A. - (1970) *Proc. 3rd Int. Conf. on Rain Erosion and Associated Phenomena*, Royal Aircraft Establishment, England, p.303.
- Field J.E., Gorham D.A. & Rickerby D.G. - (1979a) in *Erosion : Prevention and Useful Applications* ASTM STP 664, ed. Adler W.F., American Society for Testing and Materials, p.298.
- Field J.E., Gorham D.A., Hagan J.T., Matthewson M.J., Swain M.V. & van der Zwaag S. - (1979b) *Proc. 5th Int. Conf. on Erosion by Liquid and Solid Impact*, paper 13, Cambridge : Cavendish Laboratory.
- Field J.E., van der Zwaag S. & Townsend D. - (1983) *Proc. 6th Int. Conf. on Erosion by Liquid and Solid Impact*, paper 19, Cambridge.
- Gorham D.A. & Rickerby D.G. - (1975) *J. Phys. E.* **8**, p.794.
- Hagan J.T. & Swain M.V. - (1978) *J. Phys. D. : Appl. Phys.* **11**, p.2091.
- Huber M.T. - (1904) *Ann. Physik. U. Chemie* **14**, p.153.

- Hutchings I.M. & Winter R.E. - (1975) J. Phys. E. **8**, p.84.
- Johnson W. - (1972) Impact Strength of Materials, publ. Arnold, London.
- Kaye G.W.C. & Laby T.H. - (1973) Tables of Physical and Chemical Constants, 13th edn., publ. Longman, London.
- Knight C.G., Swain M.V. & Chaudhri M.M. - (1977) J. Mat. Sci. **12**, p.1573.
- Lawn B.R., Wilshaw T.R. & Hartley N.E.W. - (1974) Int. J. Fract. **10**, p.1.
- Lawn B.R. & Fuller E.R. - (1975) J. Mat. Sci. **10**, p.2016.
- Lynch C.T. - (1975) Handbook of Materials Science Vol. II, CRC Press, U.S.A.
- Matthewson M.J. - (1978) Ph.D Thesis, University of Cambridge.
- Matthewson M.J. & Field J.E. - (1980) J. Phys. E. **13**, p.355.
- Morrell R. - (1985) Handbook of Properties of Technical and Engineering Ceramics, Her Majesty's Stationery Office.
- Pope P. - (1985) Private Communication.
- Rice R.W. - (1977) Treatise on Materials Science and Technology, ed. MacCrone R.K., **11**, p.199.
- Seigel A.E. - (1965) The Theory of High-speed Guns, AGARDograph, **91**.
- Swain M.V. & Hagan J.T. - (1980) J. Mat. Sci. **15**, p.387.
- Tilly G.P. & Sage W. - (1970) Wear **16**, p.447.
- van der Zwaag S. - (1981) Ph.D Thesis, University of Cambridge.
- van der Zwaag S. & Field J.E. - (1983) Eng. Frac. Mech. **17**, p.367.
- With G. de - (1984) J. Mat. Sci. **19**, p.2195.
- Woodward A.C. & Field J.E. - (1974) 11th Int. Cong. on High-speed Photography, London.

TABLE 1

Material	$K_{IC}$ MN <sup>3/2</sup>	$\sigma_f$ MPa	Flaw size / $\mu$ m	Threshold velocity Water / m s <sup>-1</sup>	Threshold velocity Mild Steel / m s <sup>-1</sup>	Vicker's Hardness / GPa
Sapphire	1.80	362	~ 10	300 - 350	20 < vs < 23	12.0
Alumina	2.71	146	250	300 - 350	22 < vs < 25	12.0
Soda-lime-glass	0.75	100	40	150(1)	19	4.5
Hot-pressed silicon nitride	5.2	265	260	500(2)	38	16.0

(1) van der Zwaag (1981)

(2) Mathewson (1978)

TABLE 2

Material	Density $\rho/\text{kg m}^{-3}\times 10^{-3}$	Hardness $H_V/\text{GPa}$	Fracture Toughness $K_{Ic}/\text{MN}^{-3/2}$
Alumina	3.69	$11.9\pm 1.6$	$2.99\pm 0.17$
Glass ceramic	2.47	$9.2\pm 0.5$	$1.77\pm 0.12$
Boron carbide	2.52	$20.6\pm 3.3$	2.5 -5.0 <sup>(1)</sup>
Soda-lime glass	2.50	4.5	0.75
Hardened steel	7.8	10	

<sup>(1)</sup> Morrell (1985)

TABLE 3

Material	Density $\rho/10^3 \text{ kg m}^{-3}$	Longitudinal Stress Wave $C_l/\text{m s}^{-1}$	Shear Stress Wave Velocity $C_s/\text{m s}^{-1}$	Shear Modulus $G/\text{GPa}$	Bulk Modulus $K/\text{GPa}$	Young's Modulus $E/\text{GPa}$	Poisson's Ratio $\nu$
Soda-lime- glass	2.50	5600 $\pm 100$	3325 $\pm 50$	27.6 $\pm 0.8$	41.5 $\pm 2.7$	67.9 $\pm 3.0$	0.23 $\pm 0.02$
Glass ceramic	2.47	6100 $\pm 150$	3760 $\pm 50$	34.8 $\pm 0.9$	45.5 $\pm 3.4$	83.3 $\pm 4.0$	0.20 $\pm 0.03$
Alumina	3.69	8890 $\pm 300$	5415 $\pm 100$	108 $\pm 4$	147 $\pm 10$	260 $\pm 10$	0.21 $\pm 0.03$
Boron carbide	2.50	12,800 $\pm 500$	7640 $\pm 150$	146 $\pm 5$	215 $\pm 20$	360 $\pm 30$	0.22 $\pm 0.03$

## FIGURE CAPTIONS

- Fig.1 Schematic diagram of the various stages in the impact of a cylindrical jet on a solid target.
- Fig.2 a) Schematic diagram of the nozzle assembly (not to scale).  
b) The variable velocity air gun (not to scale).
- Fig.3 Impact damage produced in zinc sulphide by a 0.8 mm water jet with velocity of  $200 \text{ m s}^{-1}$ .
- Fig.4 Schematic diagram of the hydraulic pressure tester apparatus.
- Fig.5 Variation of the residual fracture stress with jet impact velocity for soda-lime glass. Jet from the 0.8 mm orifice (van der Zwaag and Field 1983):  
a) Plateau region, specimen strength comparable with unimpacted material.  
b) Transition region.  
c) All specimens damaged by impact in this region.
- Fig.6 Residual strength curves for sapphire, alumina, macro-defect-free cement, hot-pressed silicon nitride and soda-lime glass (Matthewson 1978; van der Zwaag 1981).
- Fig.7 Schematic diagram of gas gun (not to scale).
- Fig.8 Schematic diagram of specimen holder (not to scale).
- Fig.9 a) Schematic representation of the apparatus for shear wave velocity measurement.  
b) Schematic representation of the apparatus for longitudinal stress wave velocity measurement.  
c) Transit time measurement for one tile,  $t_1$ , and two tiles,  $t_2$ .
- Fig.10 Display from the storage oscilloscope of the loading pulse, channel 1, and the received pulse, channel 2, for:  
a) Shear wave velocity measurement in alumina with delay time  $t$  ( $u = 50.9 \text{ mm}$ ).  
b) Longitudinal stress wave velocity measurement in glass ceramic with delay time  $t$  ( $d_1 + d_2 + d_3 + d_4 = 38.60 \text{ mm}$ ).
- Fig.11 A  $50 \text{ mm} \times 50 \text{ mm} \times 9.8 \text{ mm}$  specimen of glass ceramic after a  $240 \text{ m s}^{-1}$  impact with a 5mm diameter hardened steel sphere.  
a) Impact face with extensive radial cracking and removal of material from lateral crack formation.  
b) Rear surface of specimen showing area of failure produced.
- Fig.12 Schematic diagram of the crack formation during the impact of a sphere upon a brittle material. The dark area corresponds to the permanent deformation of the material. Hertzian cone cracks,  $c$ , initiate near the edge of the contact area during the loading cycle. Under continued loading secondary cone cracks form. Lateral cracks,  $lc$ , occur on the unloading cycle.
- Fig.13 Schematic diagram of initiation of radial cracks,  $rc$ , before cone crack,  $c$ , propagation is completed.

- Fig.14 Semi-apex cone angle,  $\theta$ , versus impact velocity for glass ceramic. a and b are uncharacteristically small angle cone cracks (see text).
- Fig.15 Side view of stress trajectories in Hertzian stress field. Plotted for  $v = 0.33$ ,  $oa$  denotes radius of contact.
- Fig.16 Imacon sequences, with interframe time of  $4.25\mu\text{s}$ , of the impact of a 5mm diameter hardened steel sphere. The frames are numbered 1 to 8:
- Impact velocity of  $310\text{ m s}^{-1}$  on a 6mm thick specimen of soda-lime glass, s. A plume of high velocity fine particles, p, is produced by the impact. Fine particles of spalled material, m, are produced from the rear of the specimen with a maximum velocity of approx.  $250\text{ m s}^{-1}$ .
  - A  $240\text{ m s}^{-1}$  impact on a 9.8mm thick specimen, s, of glass ceramic. Jetting of fine particles, p, due to deformation of the material underneath the projectile is observed from frame 2. Cracks, c, are visible on the front face of the specimen.
- Fig.17
- Scanning electron micrograph of a 5mm diameter hardened steel sphere after impact at  $240\text{ m s}^{-1}$  on glass ceramic.
  - Impact area showing central undamaged region, u, the eroded zone, e, and the embedded glass particles, g.
  - A high magnification view of the impact area.
- Fig.18 Schematic diagram of the propagation of the crushed zone and formation of the fine particle jetting material:
- Contact velocity  $>$  propagation velocity of crushed zone (dark region).
  - Contact velocity  $<$  propagation velocity of crushed zone and jetting can occur.
- Fig.19 Imacon sequence, with transmitted illumination and an interframe time of  $0.95\mu\text{s}$ , of the crack system produced by the impact of a 5mm diameter hardened steel sphere at a velocity of  $250\text{ m s}^{-1}$  on the edge of a plate 50mm x 50mm x 5mm of a) transparent glass ceramic and b) soda-lime glass. The crack velocity in the material is estimated from the growth of the cracks labelled c. Surface defects in the material, r, are extended by the Rayleigh surface wave. The plume of fine particles, p, is also evident.
- Fig.20 Imacon sequences, with transmitted illumination and  $0.95\mu\text{s}$  interframe time, of the crack systems produced by a  $250\text{ m s}^{-1}$  impact of a 3mm diameter hardened steel sphere on a) transparent glass ceramic (6mm x 50mm x 5mm) and b) soda-lime glass (12mm x 50mm x 5mm). The rear surface cracks, s, are caused by reflection of the compressive loading pulse as a tensile surface wave. Lateral cracks, l, are formed which reach the surface of the specimen resulting in material removal. The plume of fine particles, p, and the surface defects, r, extended by the Rayleigh surface wave are also evident.
- Fig.21 Imacon sequences of a 5mm diameter hardened steel sphere impact on aluminium. The specimen is labelled "s" and the frames numbered 1 to 8:
- Impact velocity of  $160\text{ m s}^{-1}$ , interframe time  $17.2\mu\text{s}$ . The impact occurs between frames 2 and 3. Ball rebounds from frame 3 onwards with a velocity of  $60 \pm 5\text{ m s}^{-1}$ . Note the flattened surface of the projectile, F, after impact. Material is expelled from the rear of the specimen after impact. In the photographs, this appears as an apparent increase in specimen thickness.
  - Impact velocity of  $295\text{ m s}^{-1}$ , interframe time  $4.25\mu\text{s}$ . The projectile fractures on impact. Cracks, C, are observed in the rear surface of the specimen from frame 6 onwards.

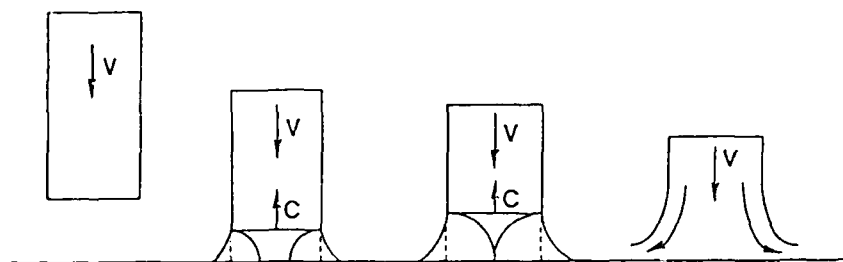


- Fig.22 Scanning electron micrograph of a 5mm diameter hardened steel sphere after impact at  $200 \text{ m s}^{-1}$  on alumina. A flat, f, is formed on the projectile and cracks, c, are observed.
- Fig.23 Schematic diagram of the failure observed in a hardened steel sphere after impact on alumina. An inverted cone, n, is formed in the sphere and fracture planes, r. The arrows indicated the radial movement of material observed with high velocity impacts.
- Fig.24 Scanning electron micrographs of the fragments of a hardened steel sphere produced by impact on an alumina tile at a velocity of  $275 \text{ m s}^{-1}$ :
- a) Cross-section of the sphere showing fracture plane, c, the flat, f, the flow lines, l, and the region, n, of the inverted cone.
  - b) High magnification of the impact area shown in a).
  - c) The inverted cone of material produced in the sphere by the impact.
- Fig.25 Scanning electron micrographs of a hardened steel sphere after impact at  $460 \text{ m s}^{-1}$  on an alumina specimen:
- a) The contact area between sphere and specimen showing the base of the inverted cone, n, and extensive radial, q.
  - b) Side view of specimen shown in a).
- Fig.26 Impact damage produced in a 50mm x 50mm x 10.5mm specimen of Sintox alumina by a 5mm diameter hardened steel sphere impact at a velocity of  $250 \text{ m s}^{-1}$ :
- a) Impact face.
  - b) Rear surface of specimens showing the area of failure due to cone crack formation.
  - c) The cone of material produced by the impact. The upper portion of the cone corresponds to the propagation of the Hertzian crack. Interaction between the reflected tensile wave and the cone crack produces the roughening on the lower portion of the cone. The line of interaction between the cone crack and reflected wave is indicated, y.
- Fig.27 Impact damage produced in a 50mm x 50mm x 8.6mm piece of Sintox alumina by a hardened steel sphere impact at a velocity of  $225 \text{ m s}^{-1}$ :
- a) Impact face.
  - b) Rear face of specimen illustrating area of cone failure.
  - c) Cross-section of specimen through the impact area. The line of interaction between the crack front and the reflected tensile wave is indicated, y.
  - d) Cone of material produced by the impact with upper smooth face and lower roughened face. The onset of the interaction between the reflected tensile wave and the propagating cone crack is shown at position y. Fracture of the cone occurred along the line of interaction.
  - e) Cross-section of specimen with cone of material.
  - f) Plan view of the alumina cone produced by the impact.
- Fig.28 Schematic representation of the cone crack with the reflected tensile wave.
- Fig.29 Semi-apex cone angle,  $\theta$ , versus impact velocity for alumina.
- Fig.30 Imacon sequences of a 5mm diameter hardened steel sphere impact with an interframe time of  $4.25\mu\text{s}$ . The frames are numbered 1 to 8:
- a) Impact velocity of  $265 \text{ m s}^{-1}$  on an alumina specimen, s. The projectile fracture on impact.

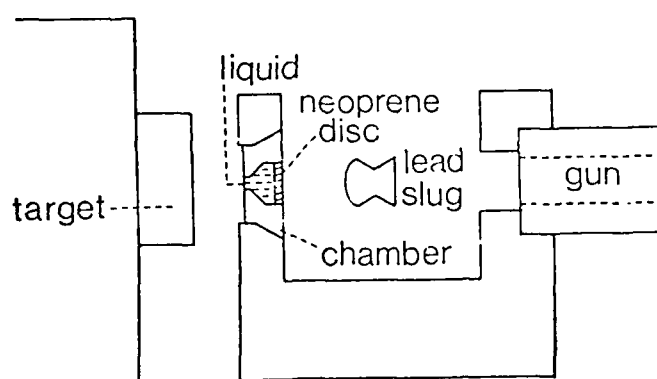
- b) An impact at a velocity of  $255 \text{ m s}^{-1}$  on boron carbide. Failure of the ball, f, occurs on impact. Cracks, c, on the impact face of the material can be observed in frames 4 to 8.

Fig.31 A 50mm x 50mm x 6.7mm specimen of boron carbide after  $255 \text{ m s}^{-1}$  impact with a 5mm diameter hardened steel sphere:

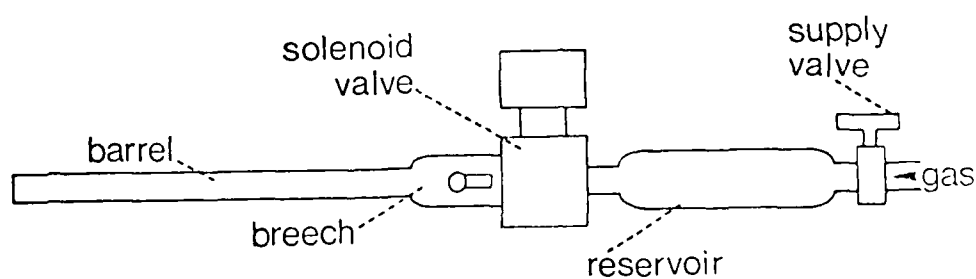
- a) Impact face showing extensive radial cracking.
- b) Rear surface of specimen.
- c) Cross-section of specimen through the impact area. V denotes the impact direction of the projectile.



**1**



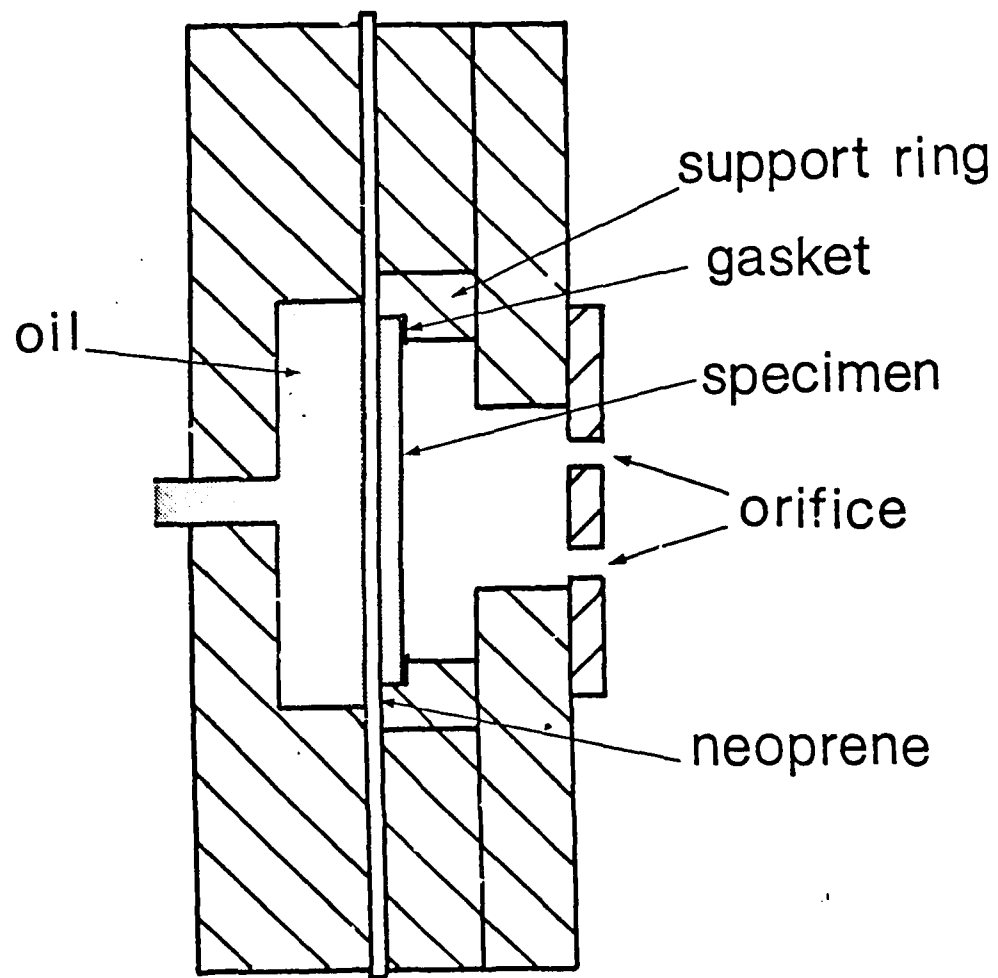
**2a**

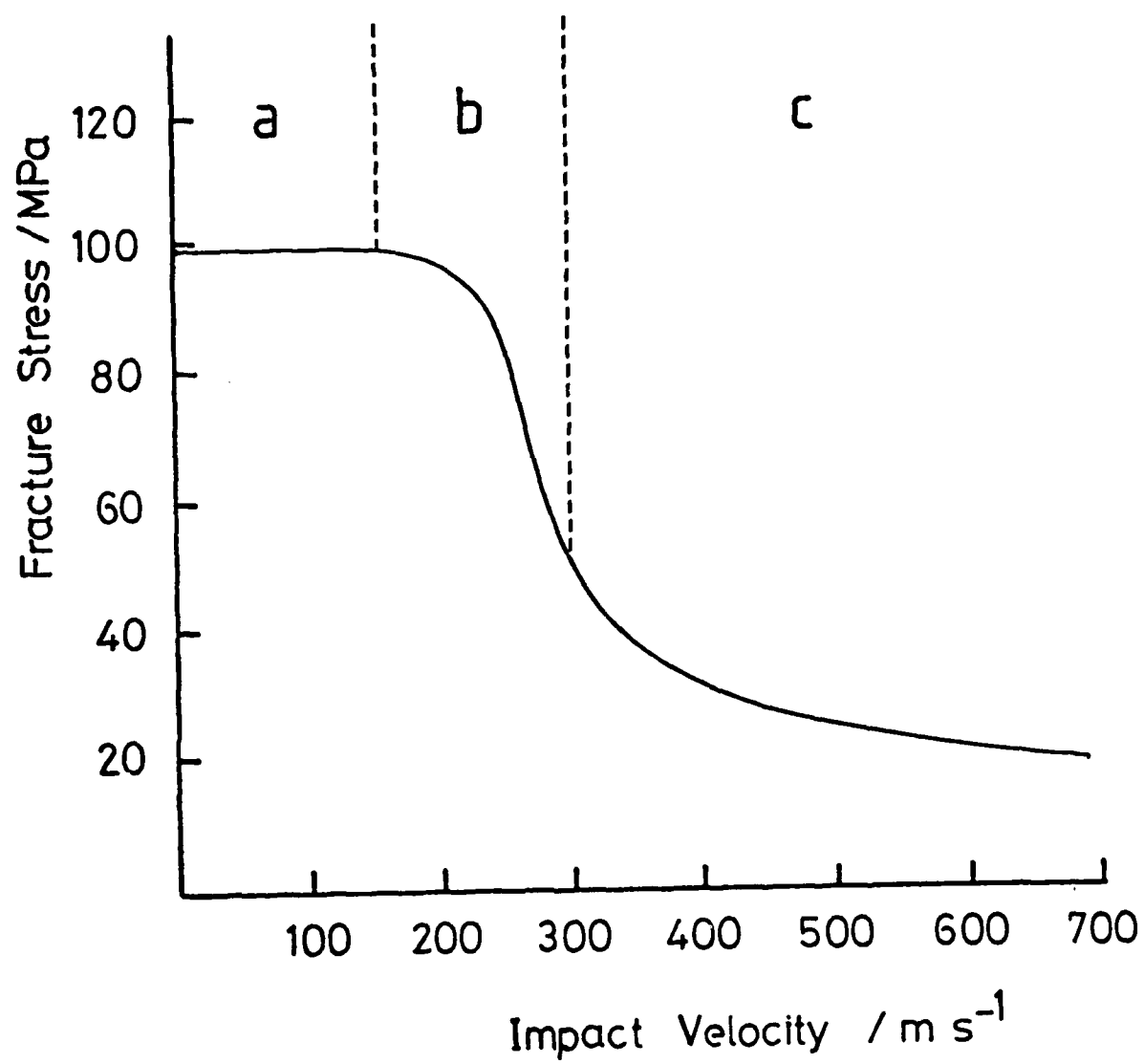


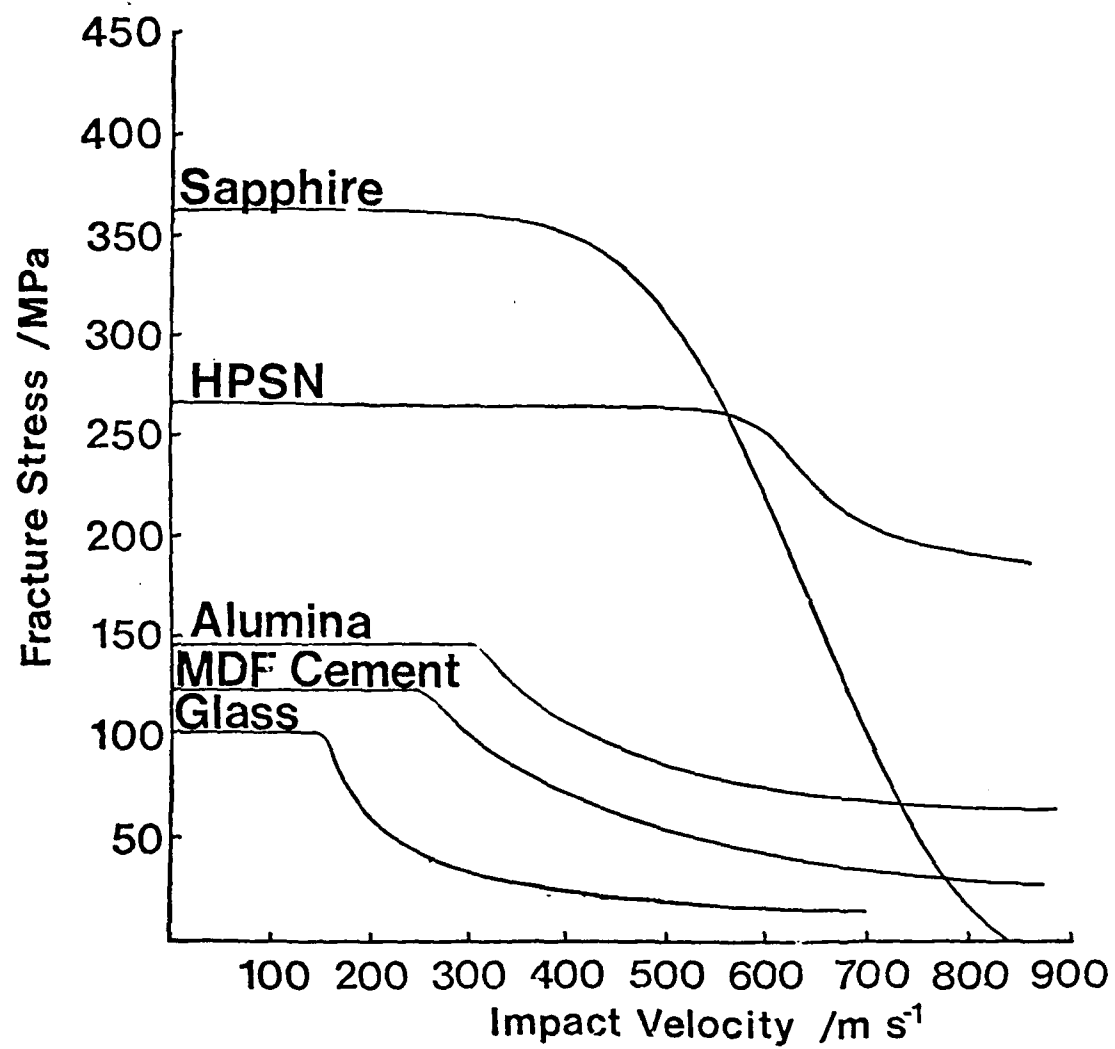
**2b**

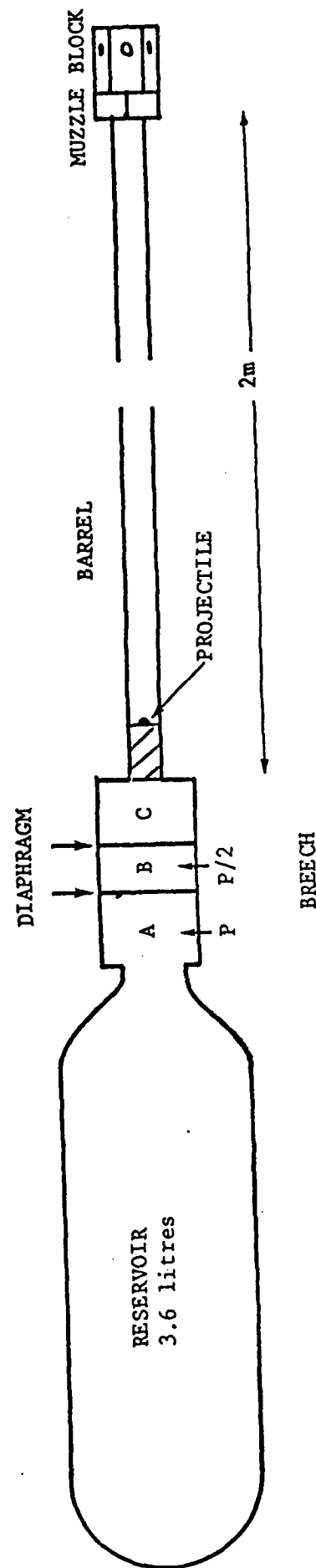
a

1 mm



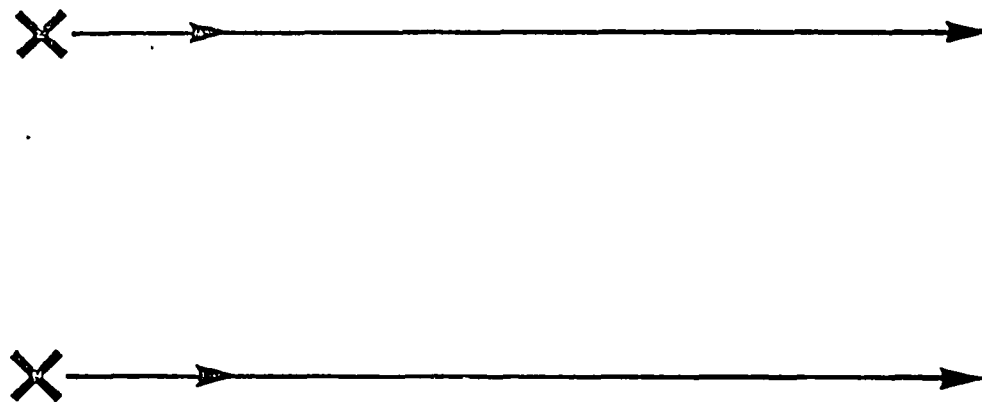




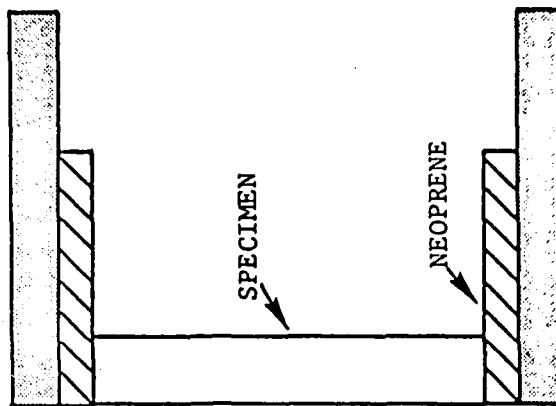




LASER BEAMS



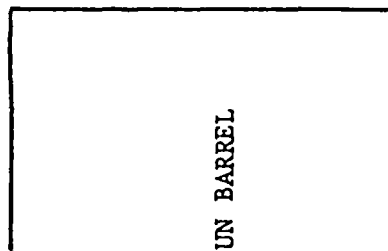
MILD STEEL SUPPORT

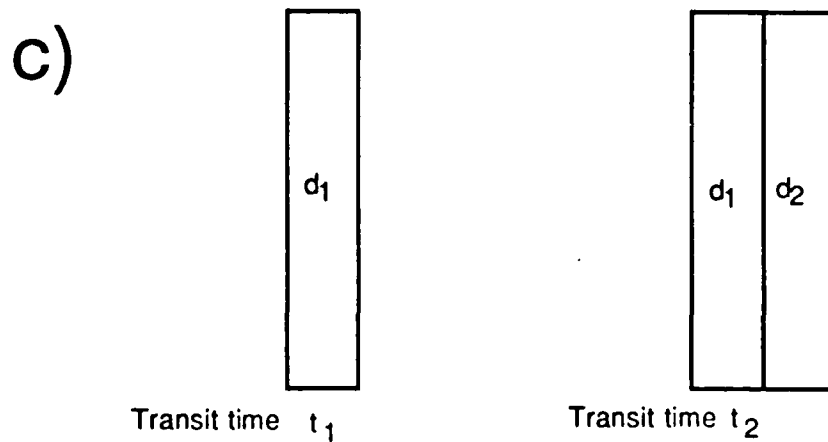
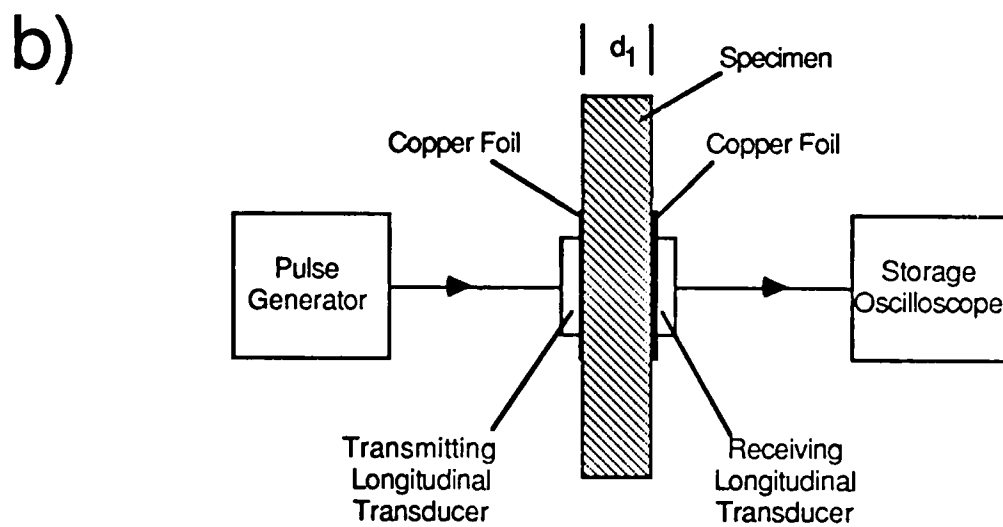
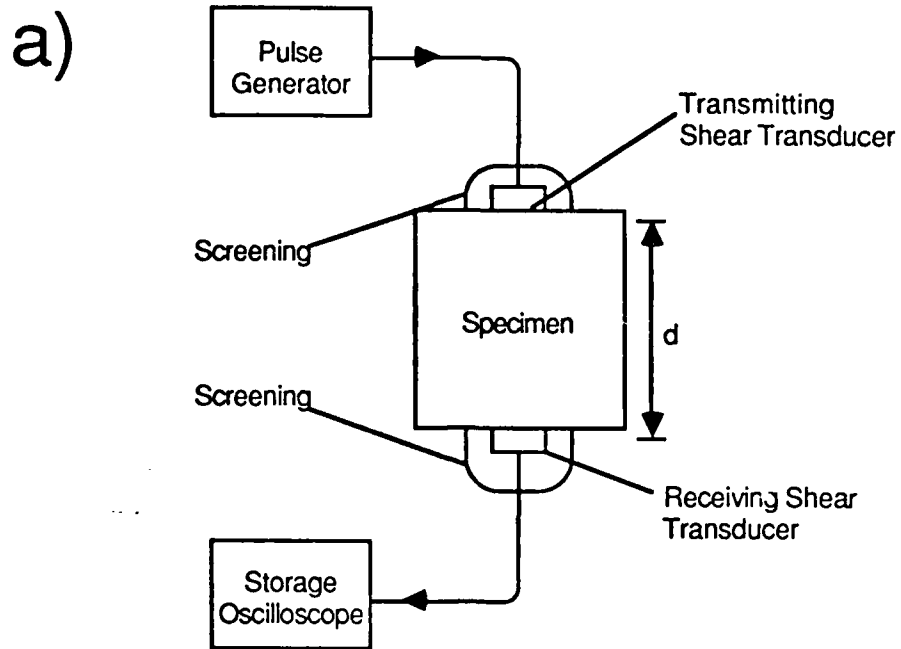


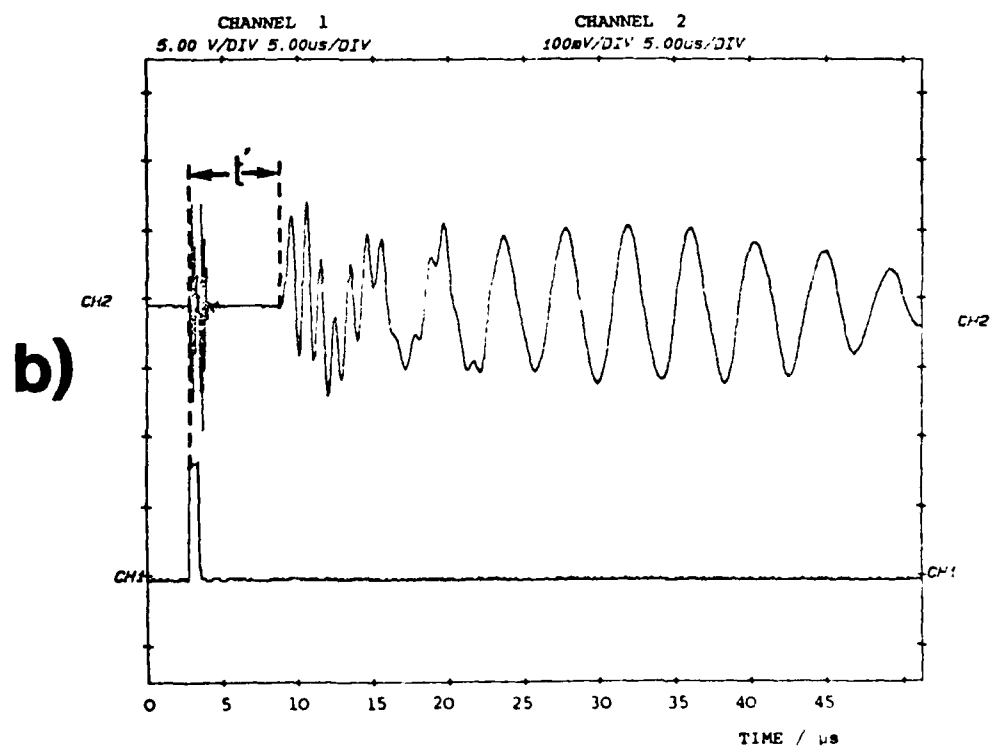
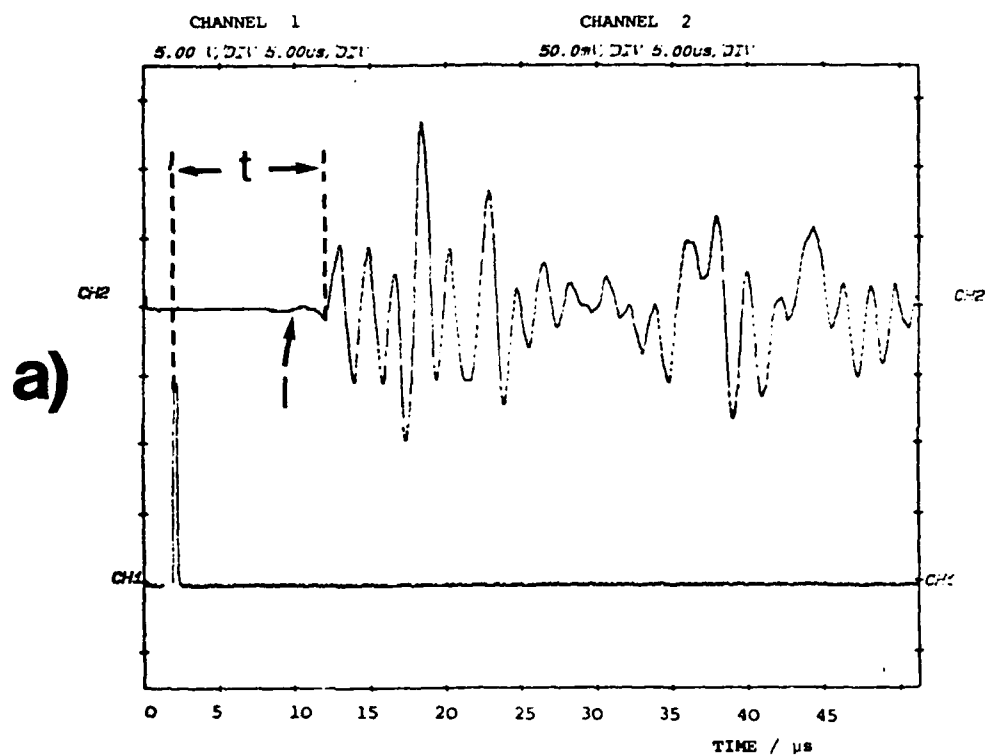
PROJECTILE

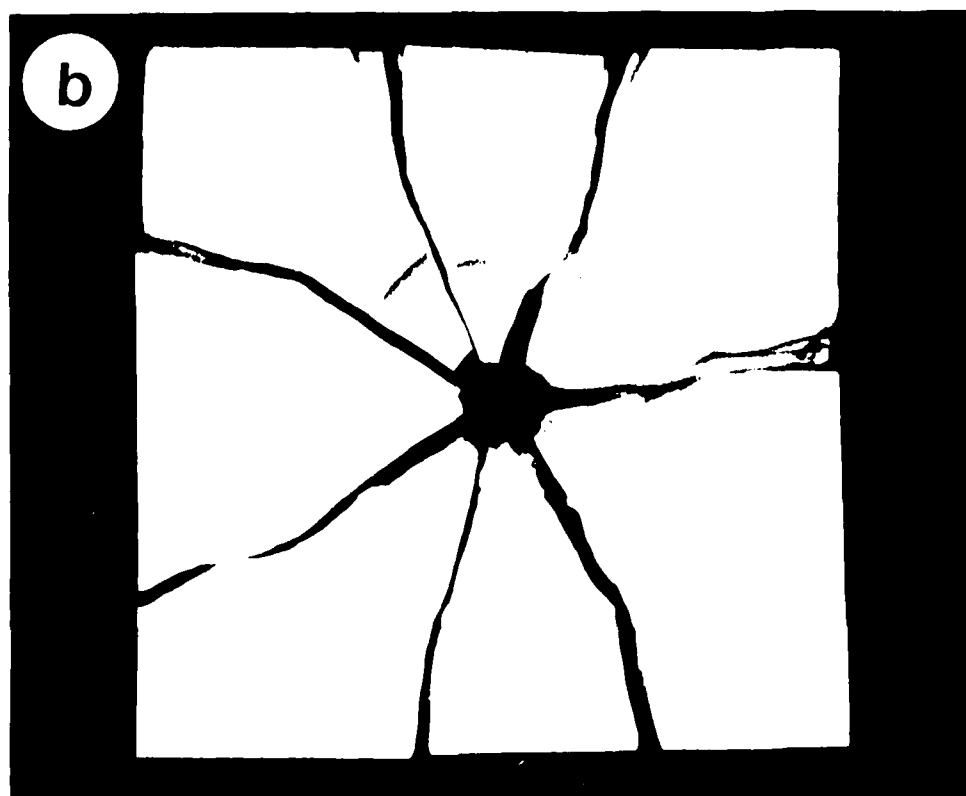


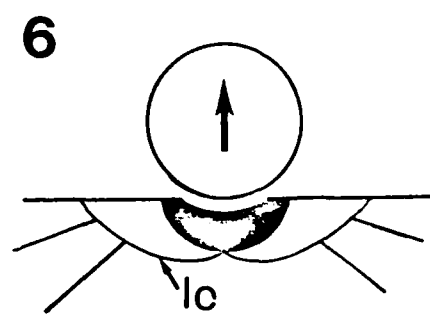
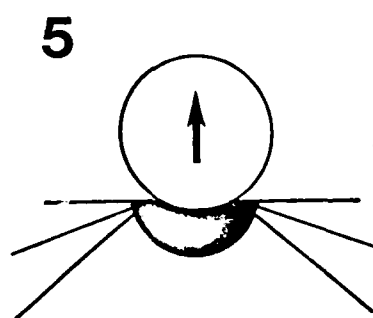
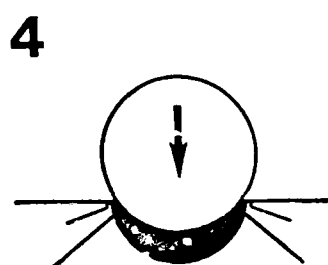
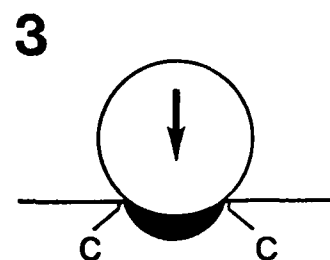
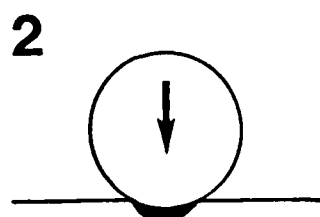
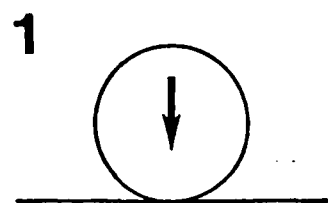
GUN BARREL

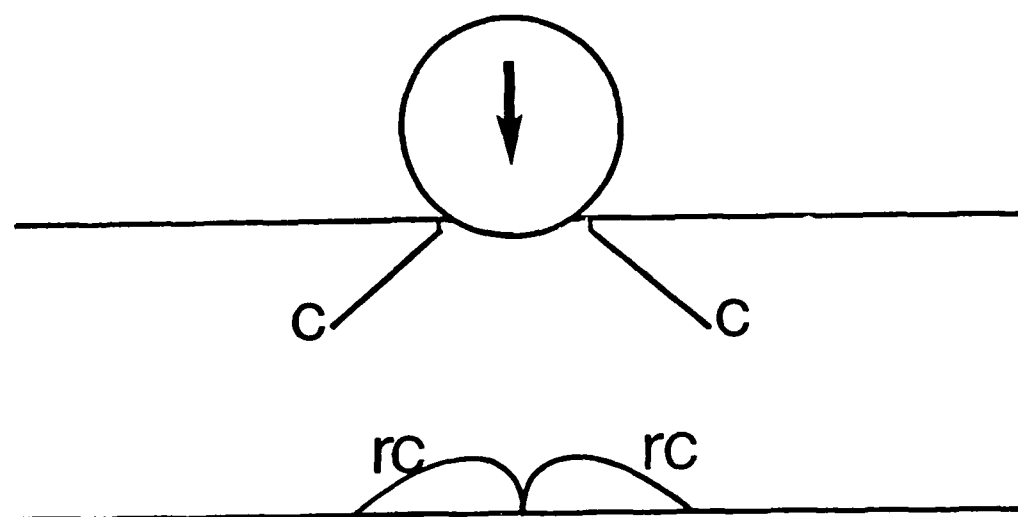


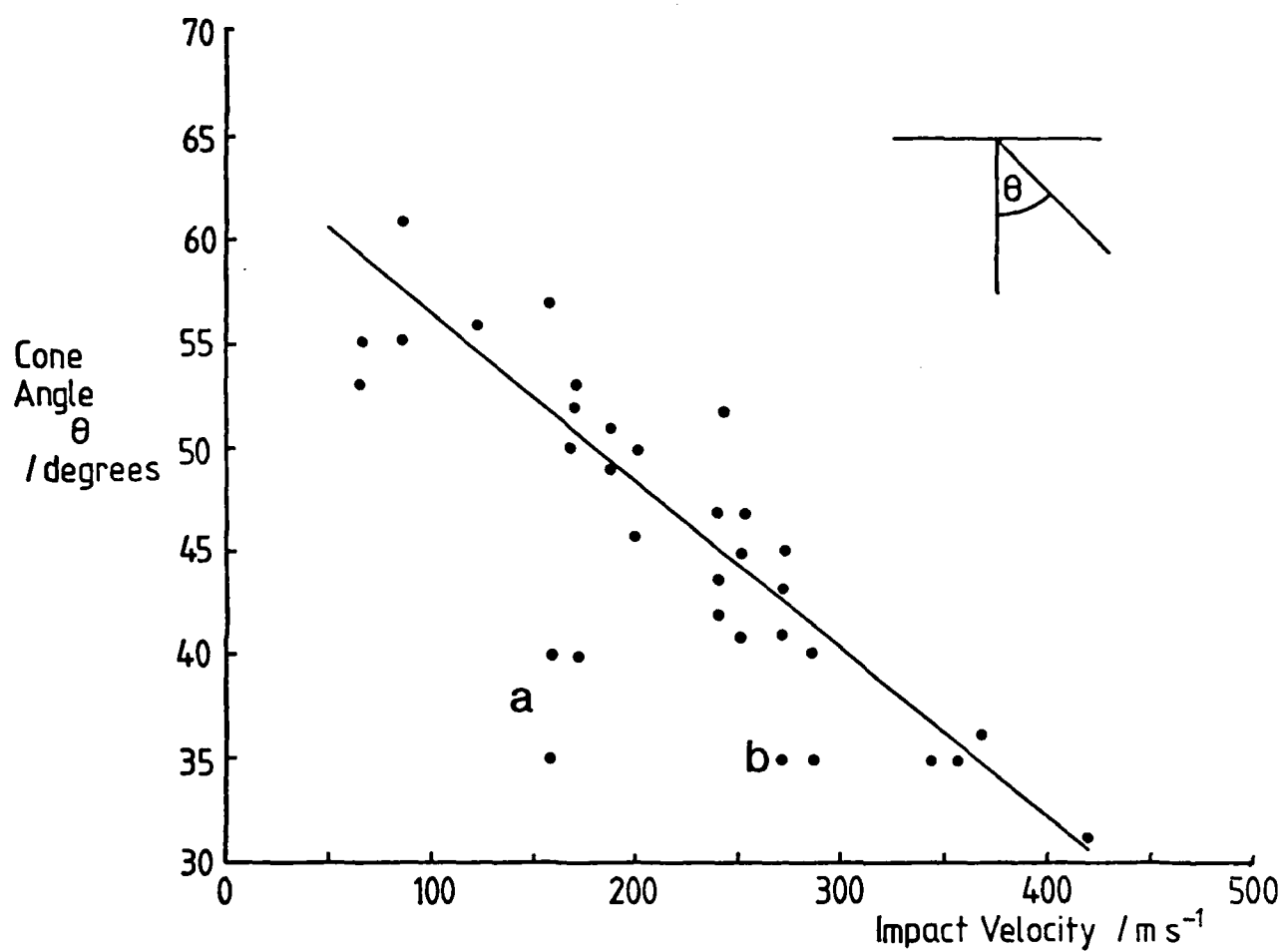


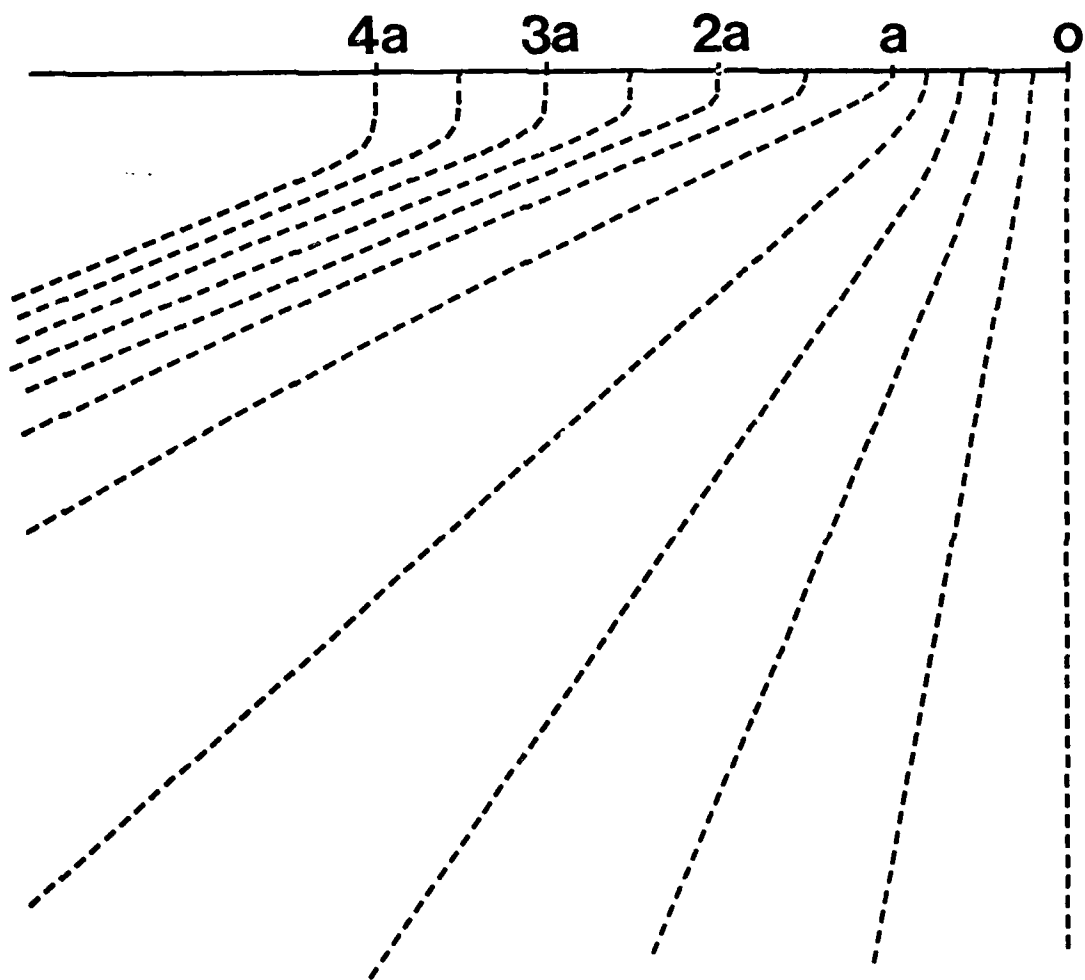




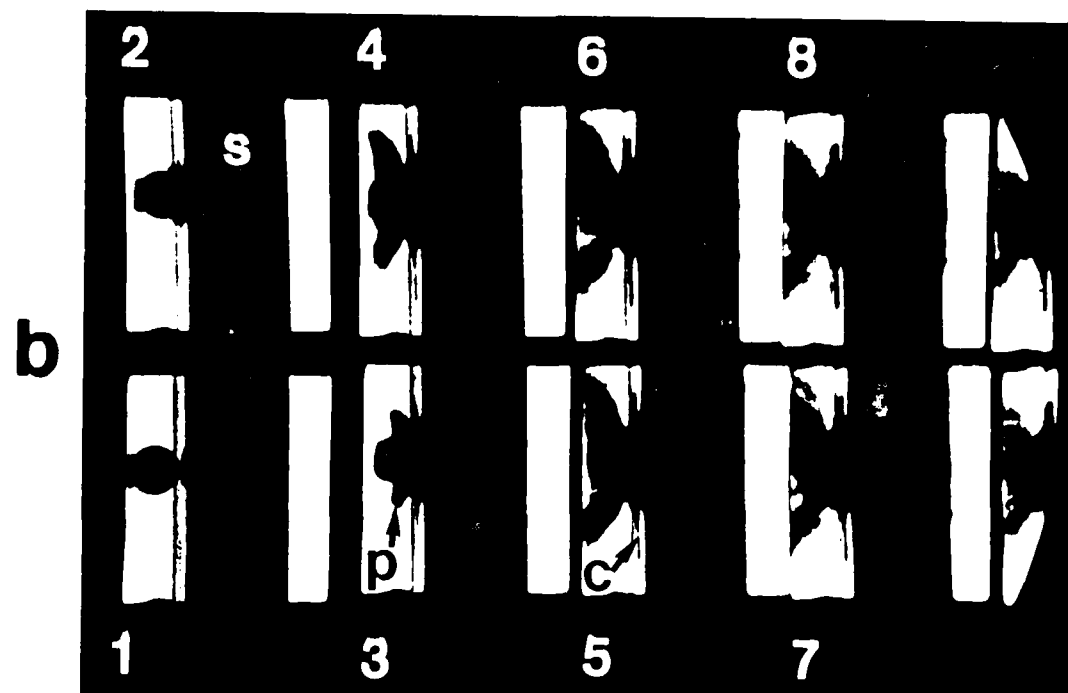
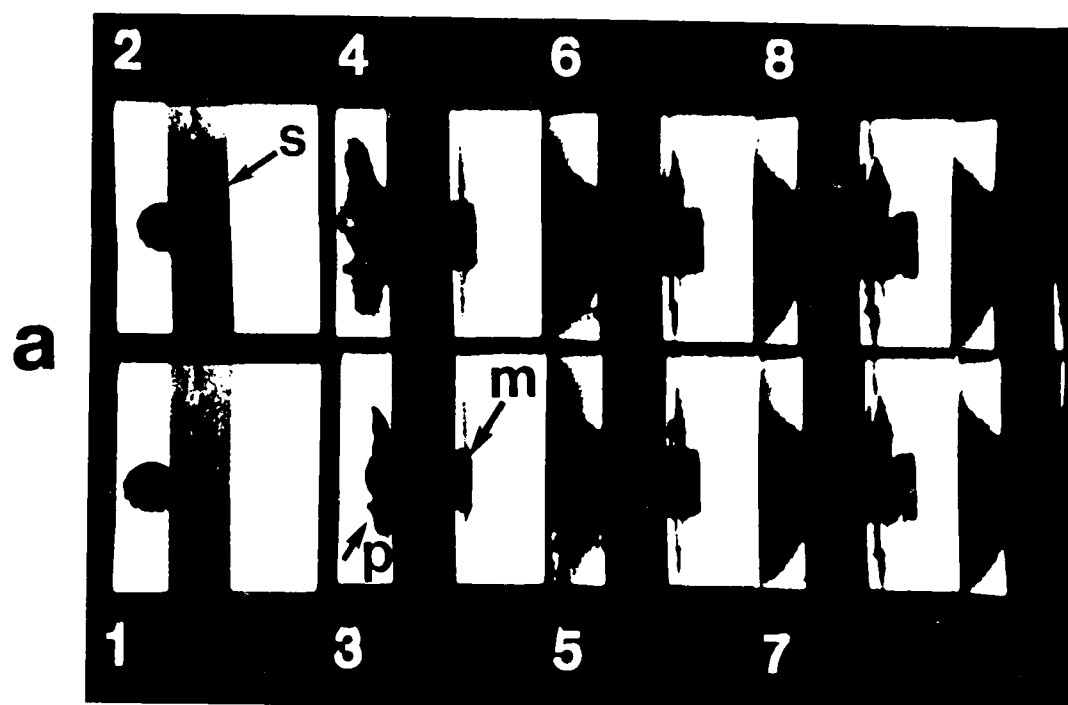


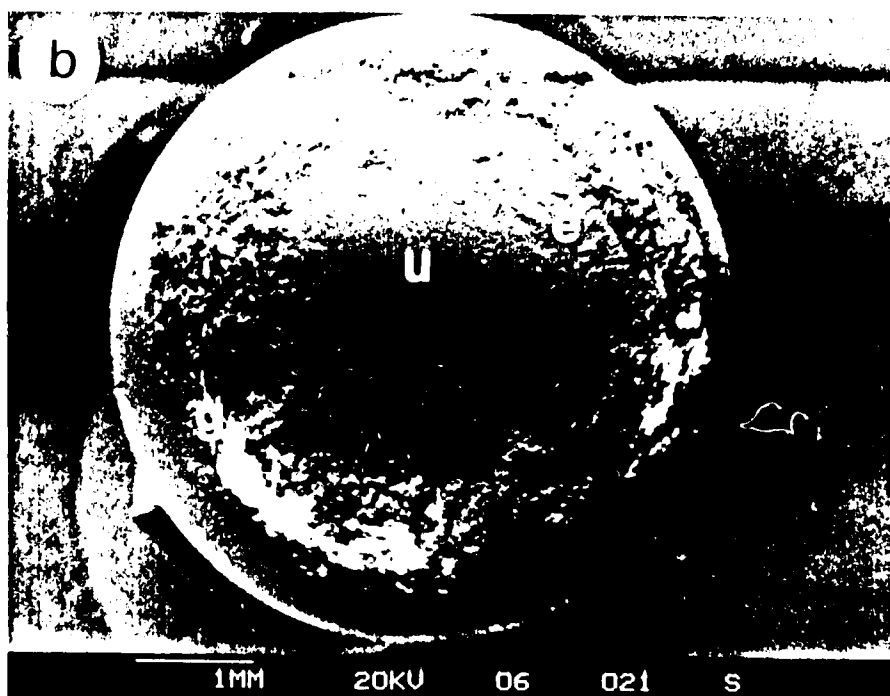
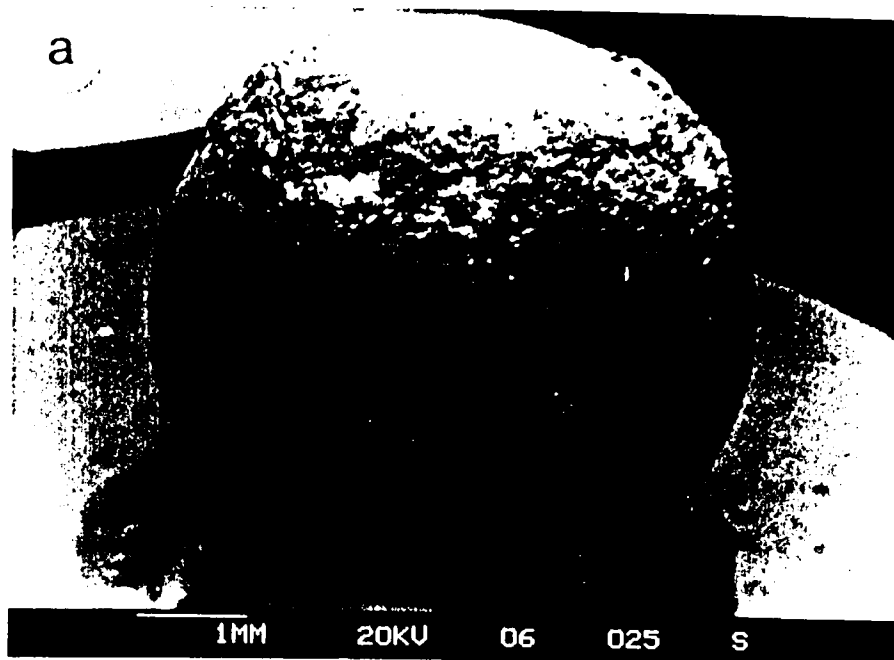




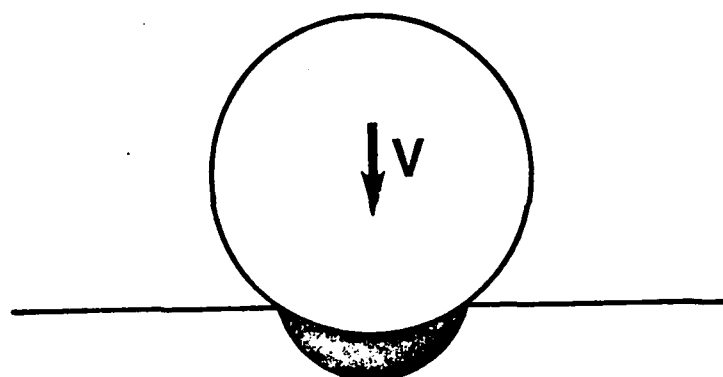




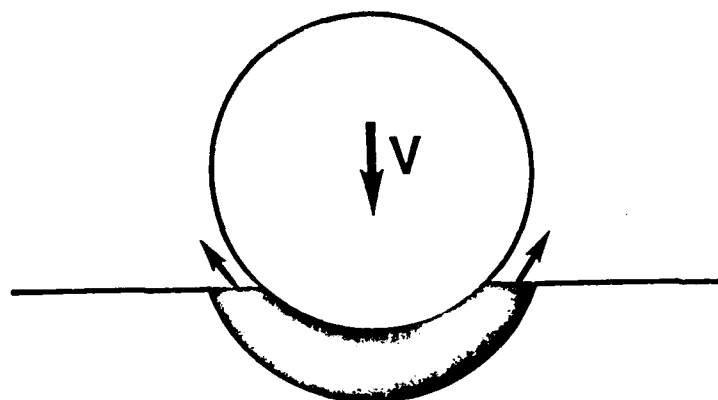


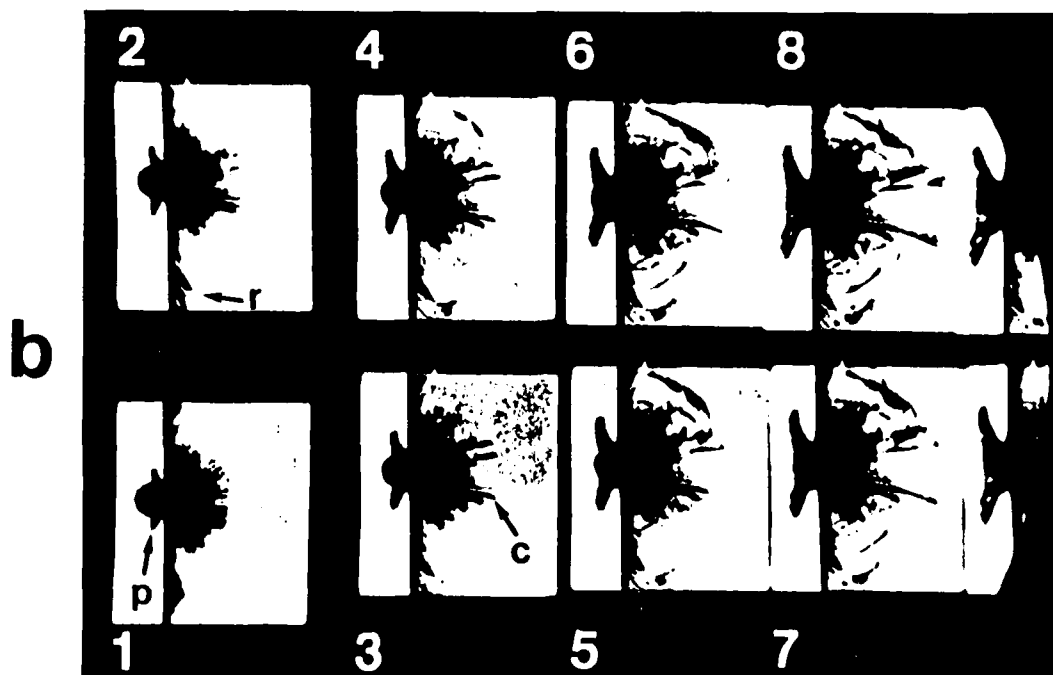
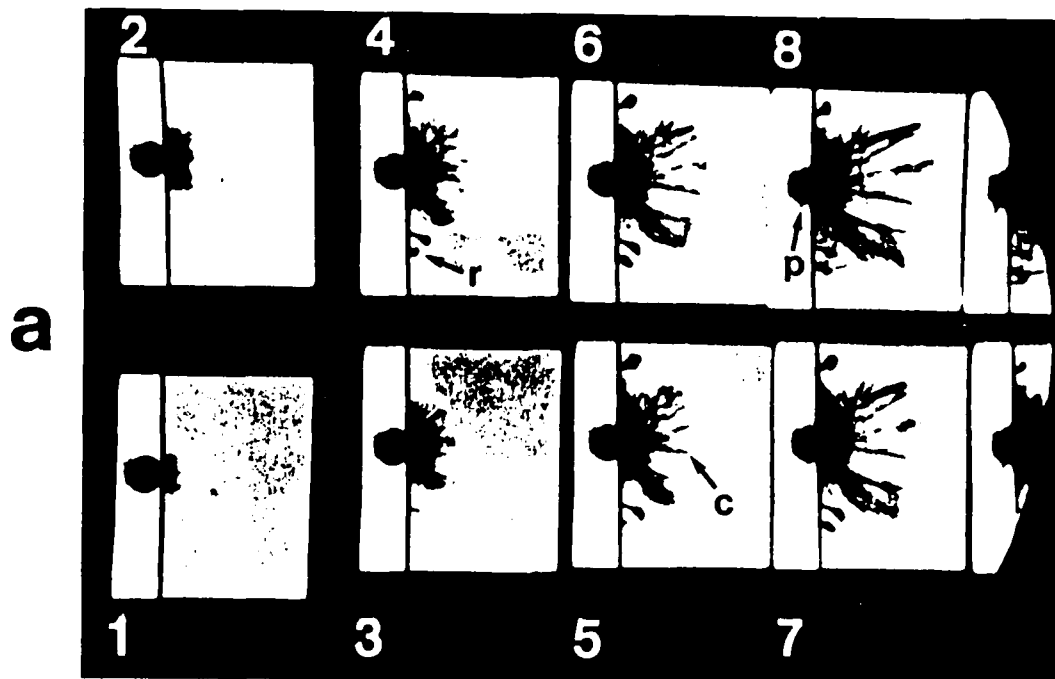


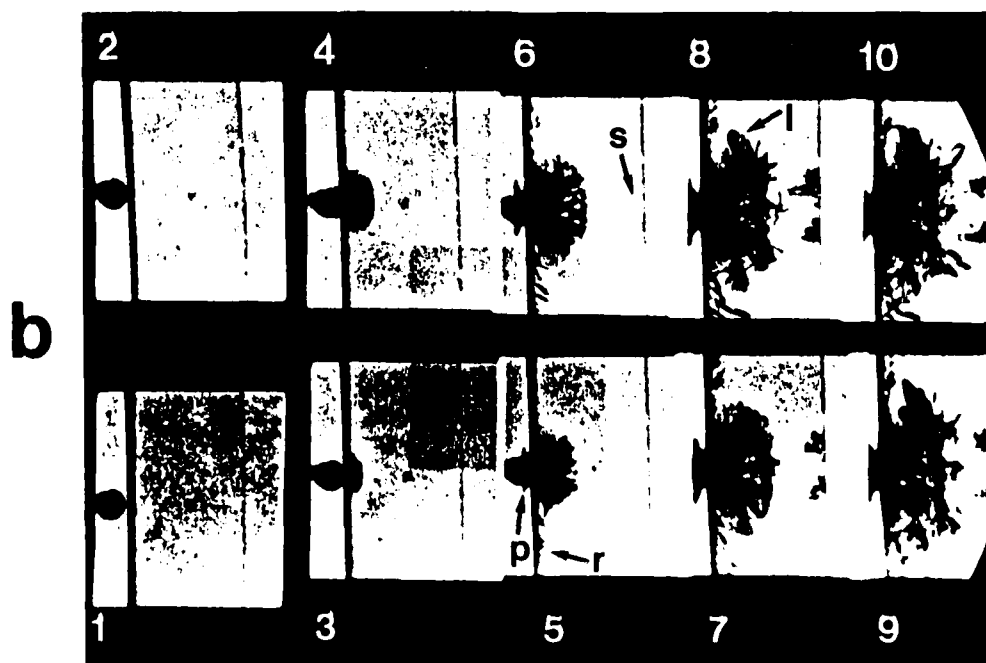
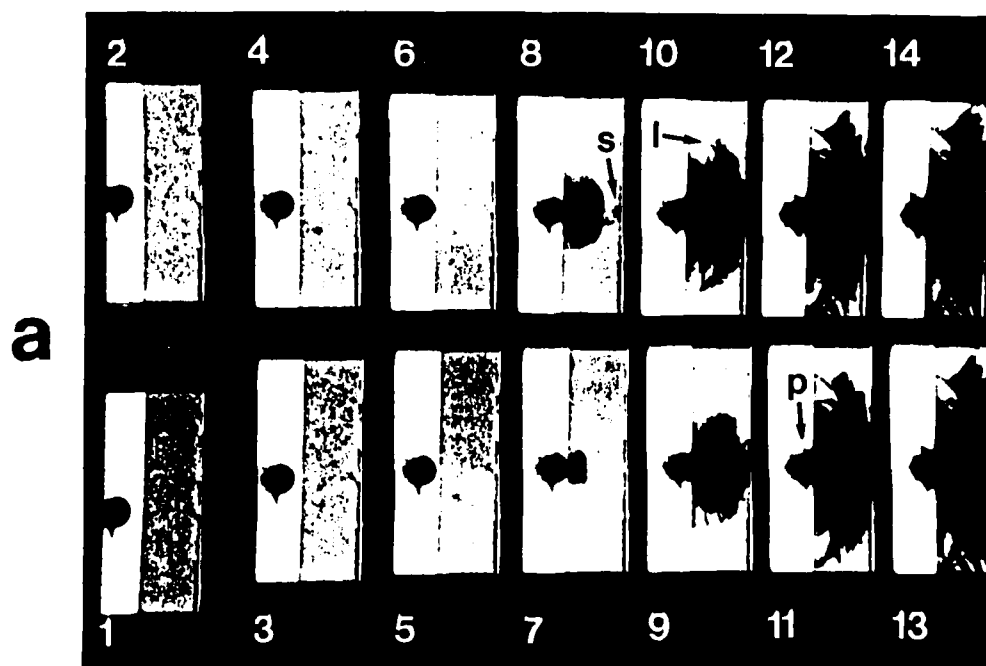
a)



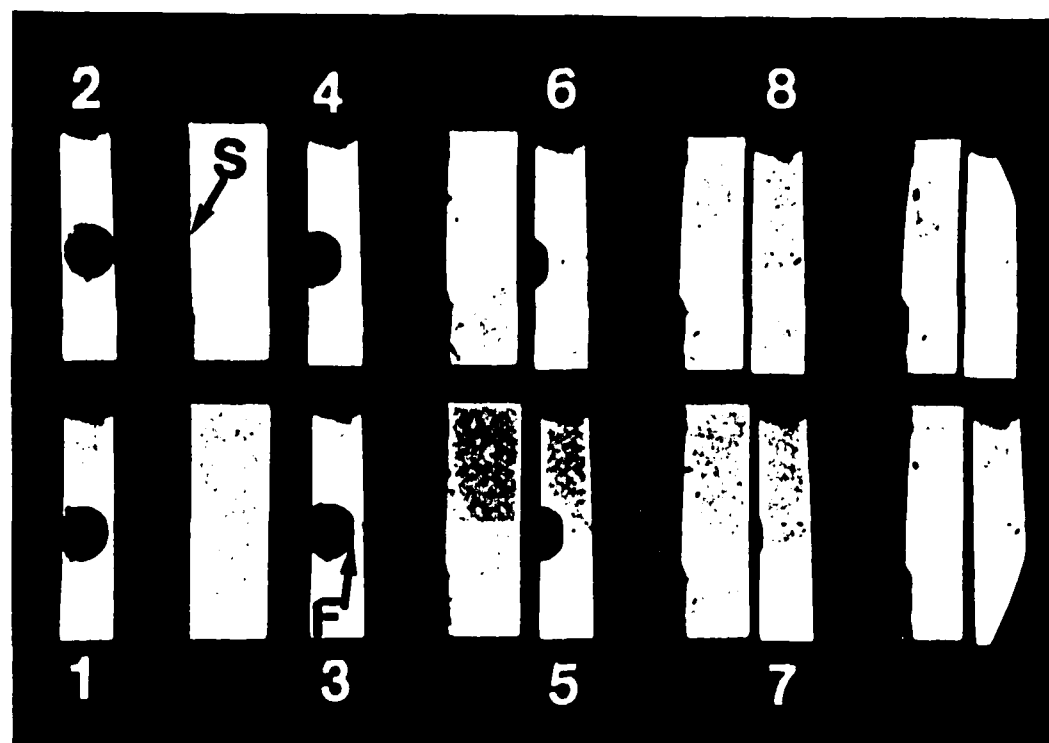
b)



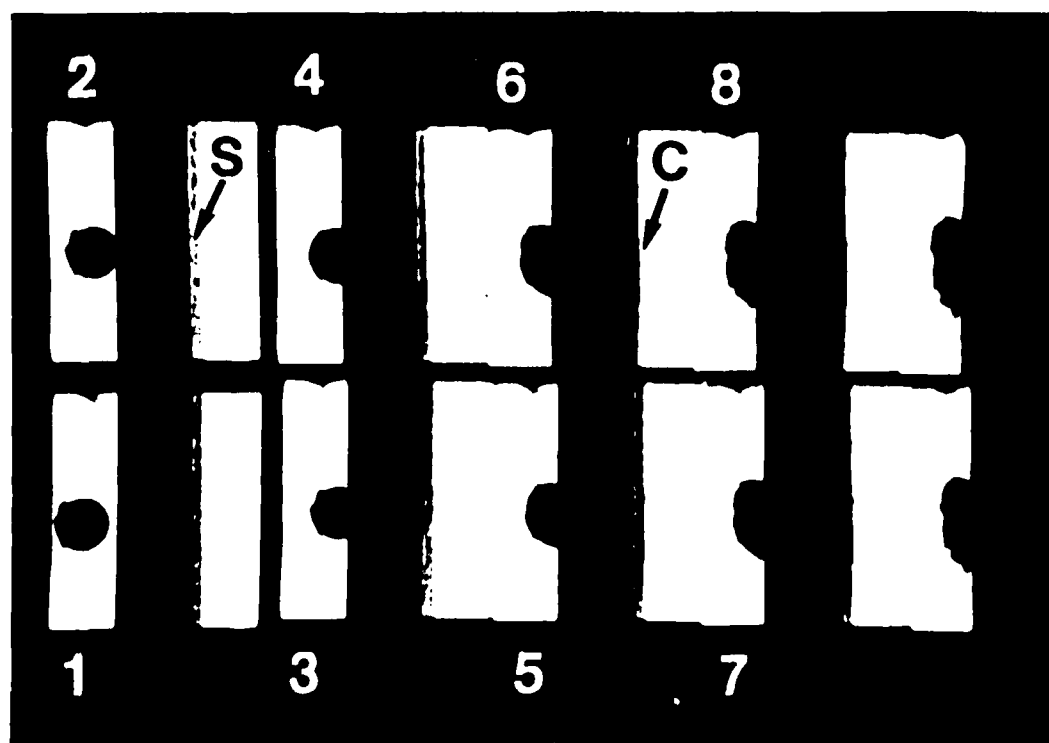


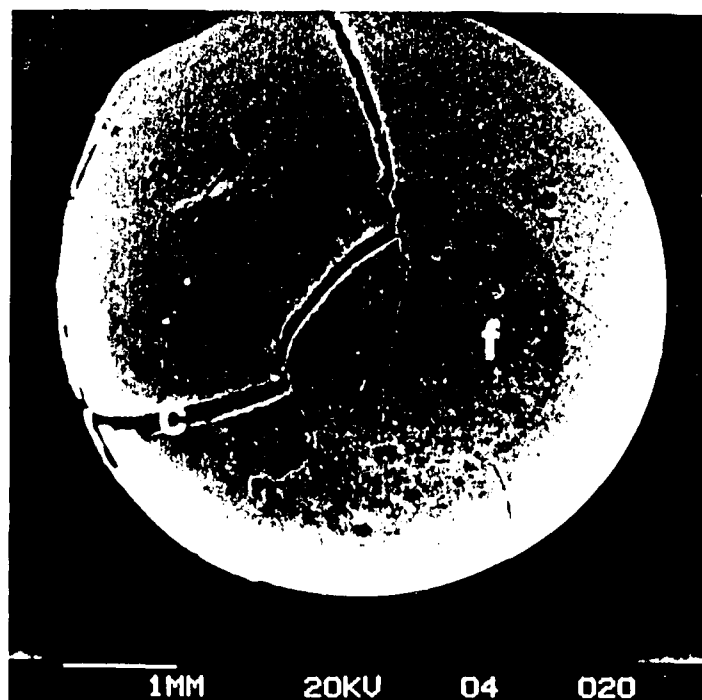


**a**

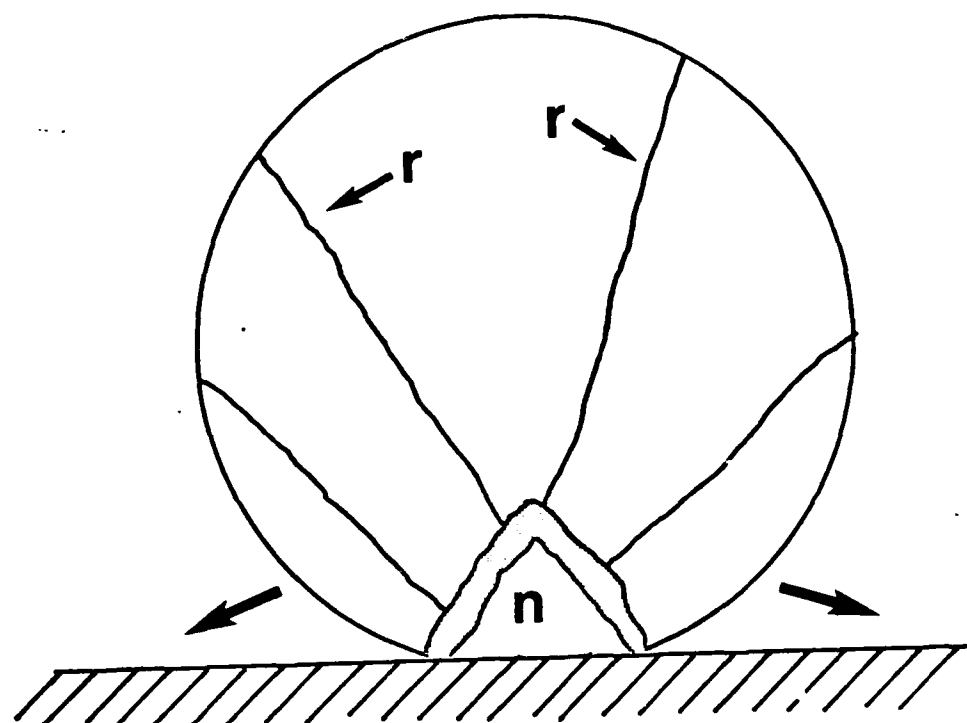


**b**

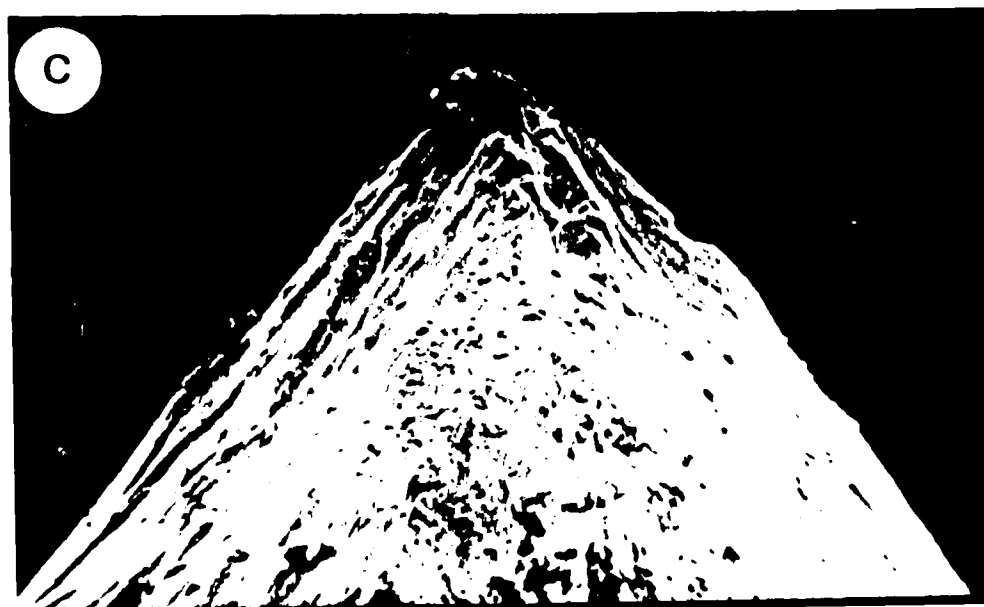
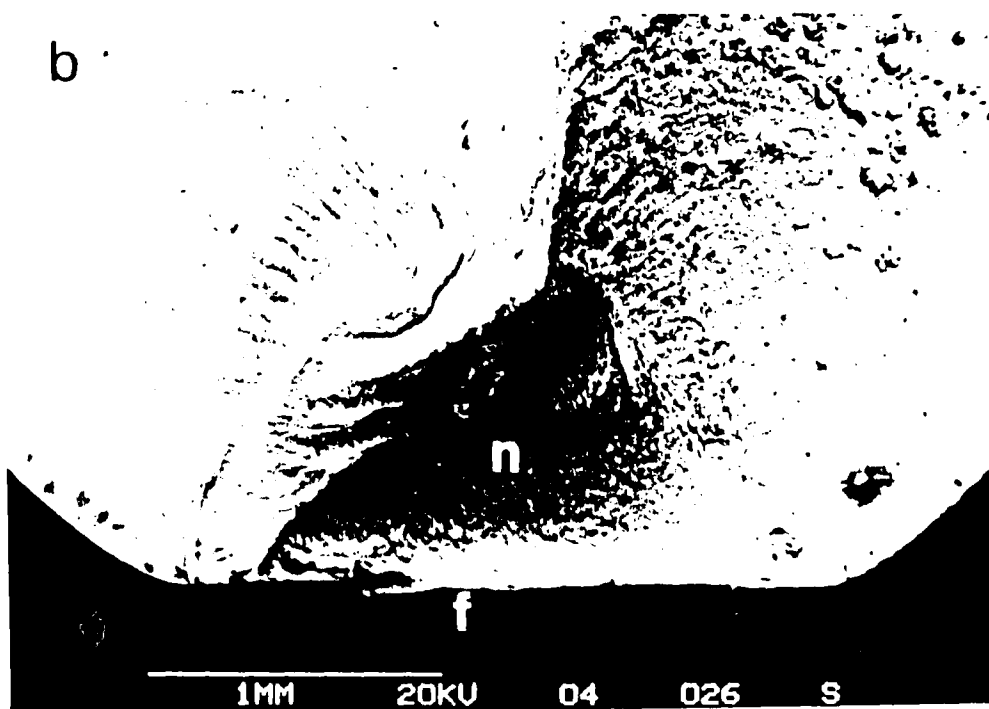
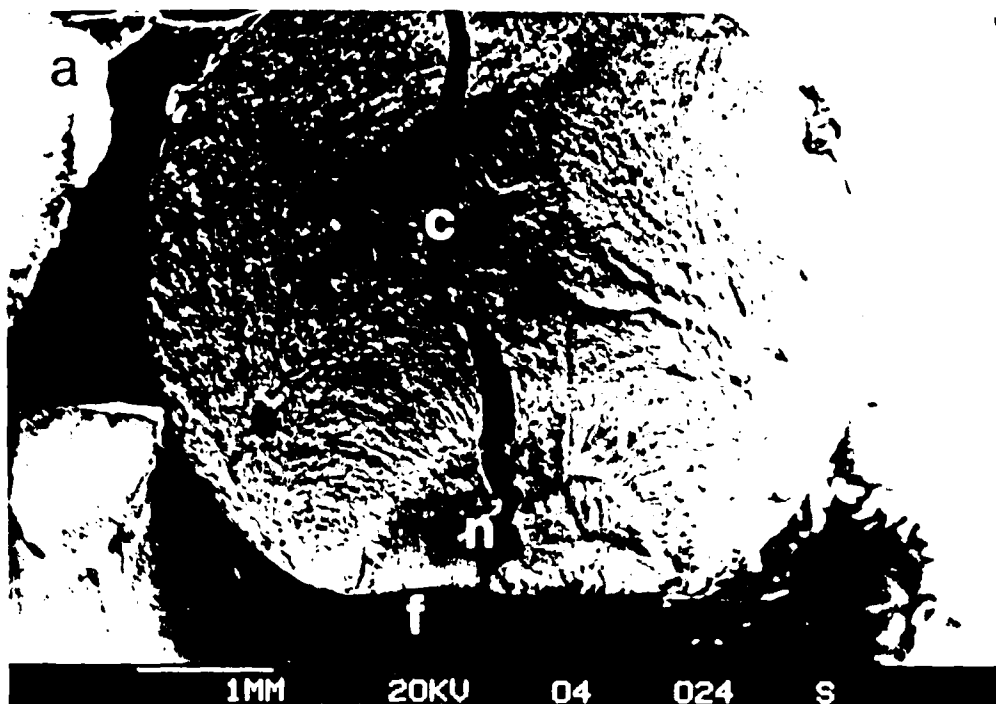


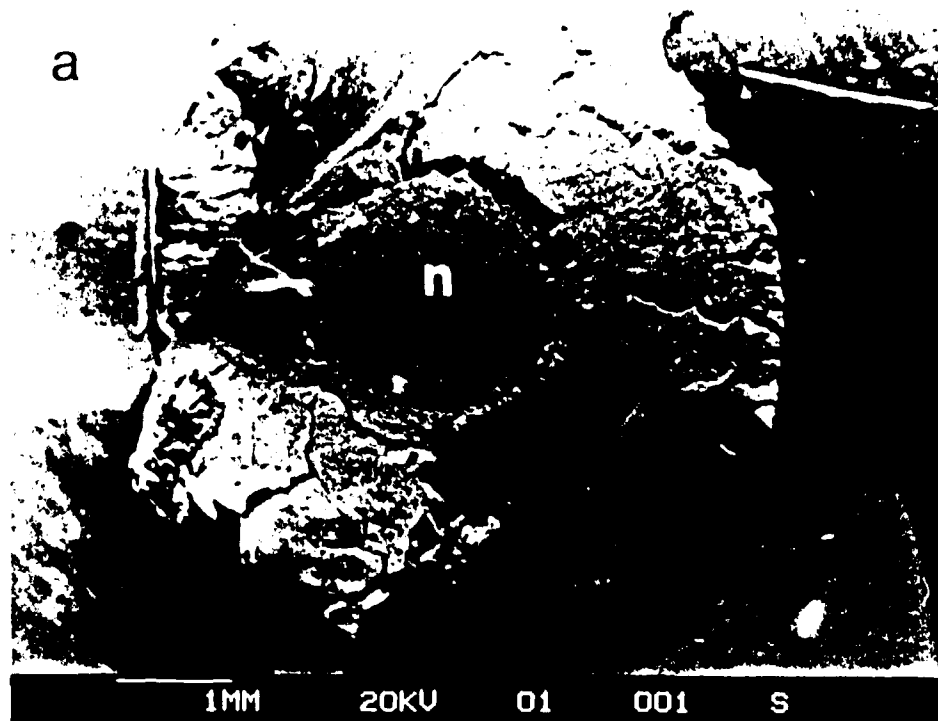


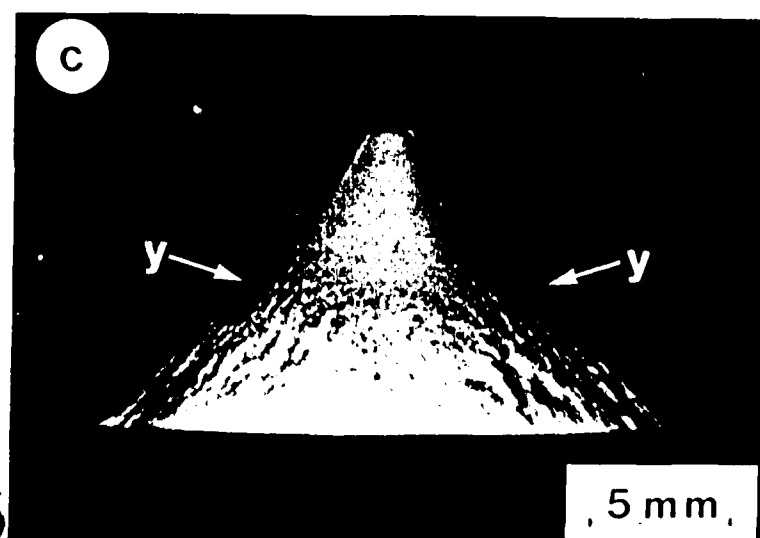
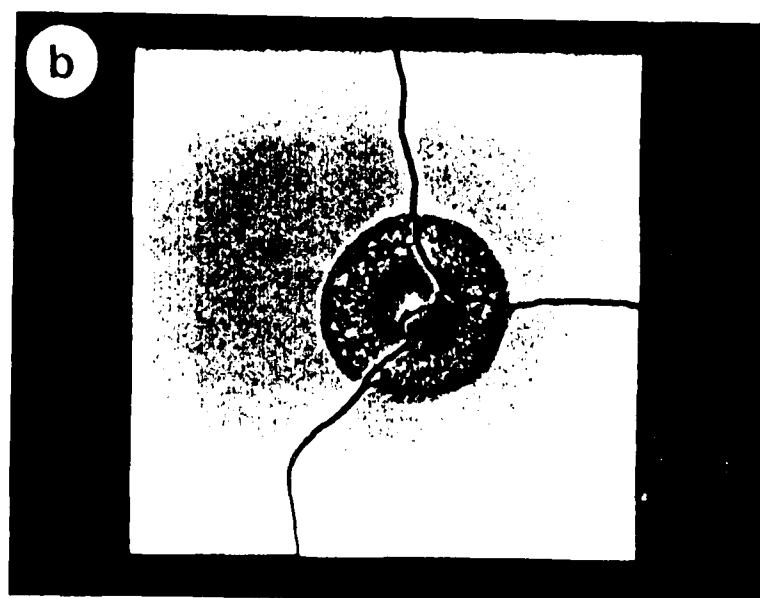
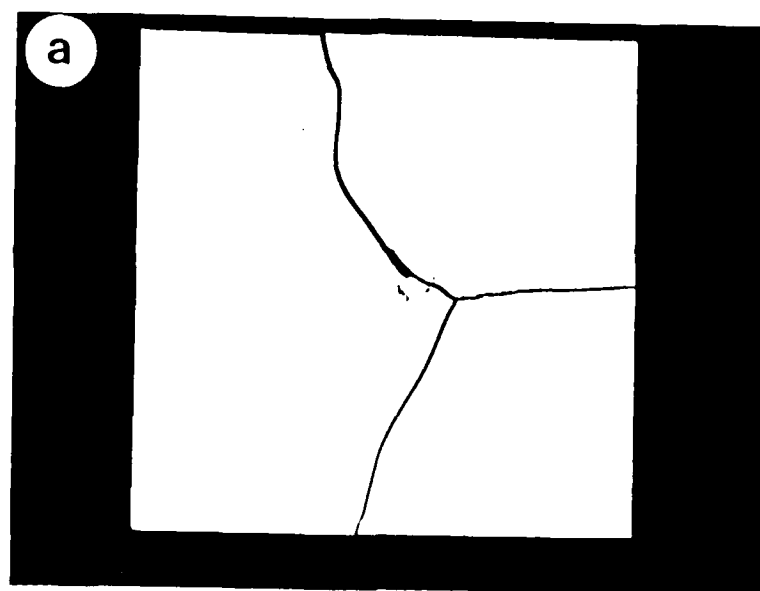
22

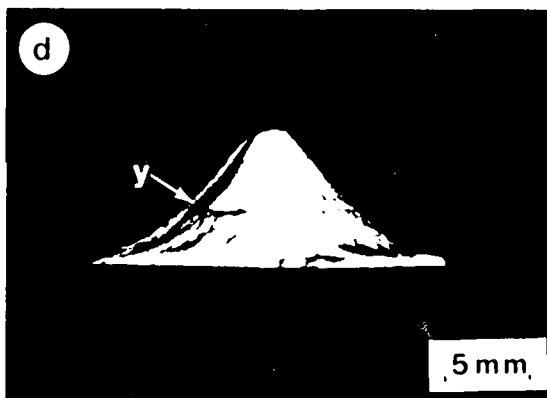
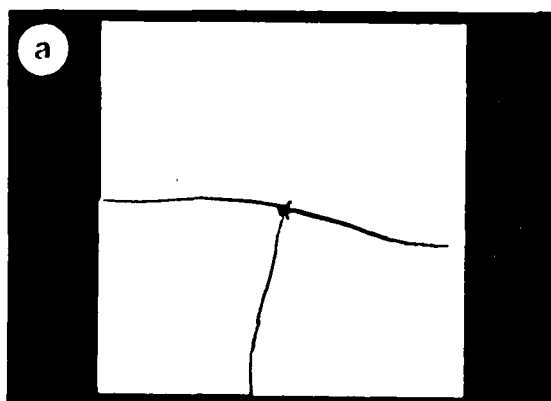




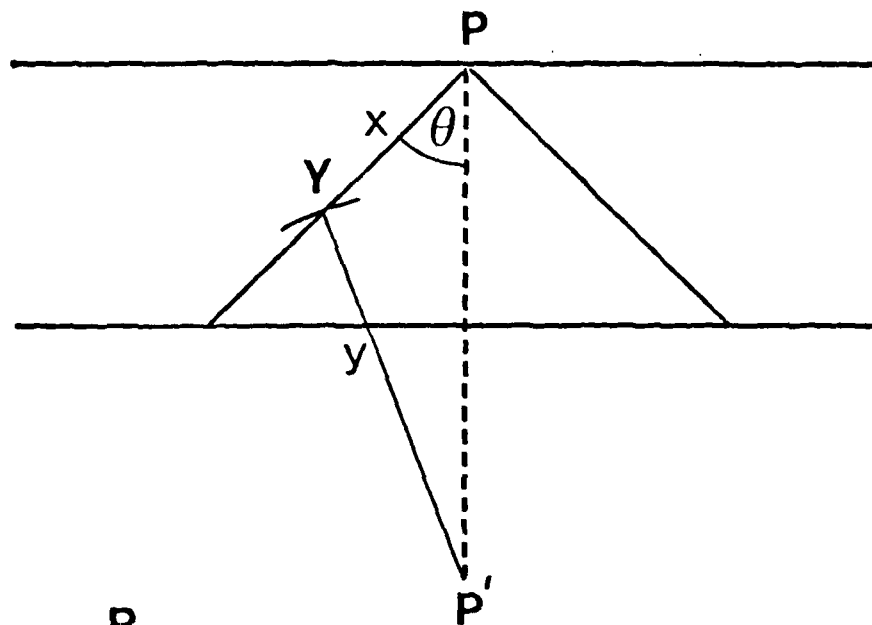




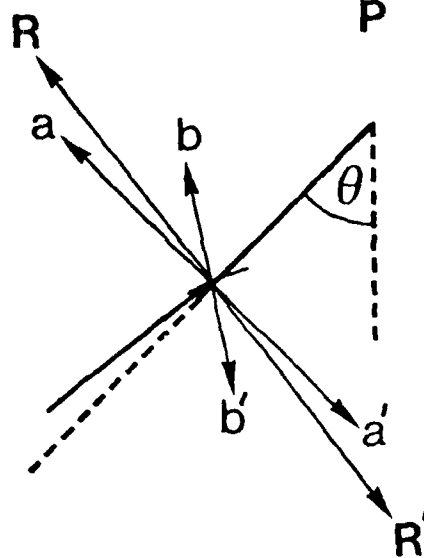


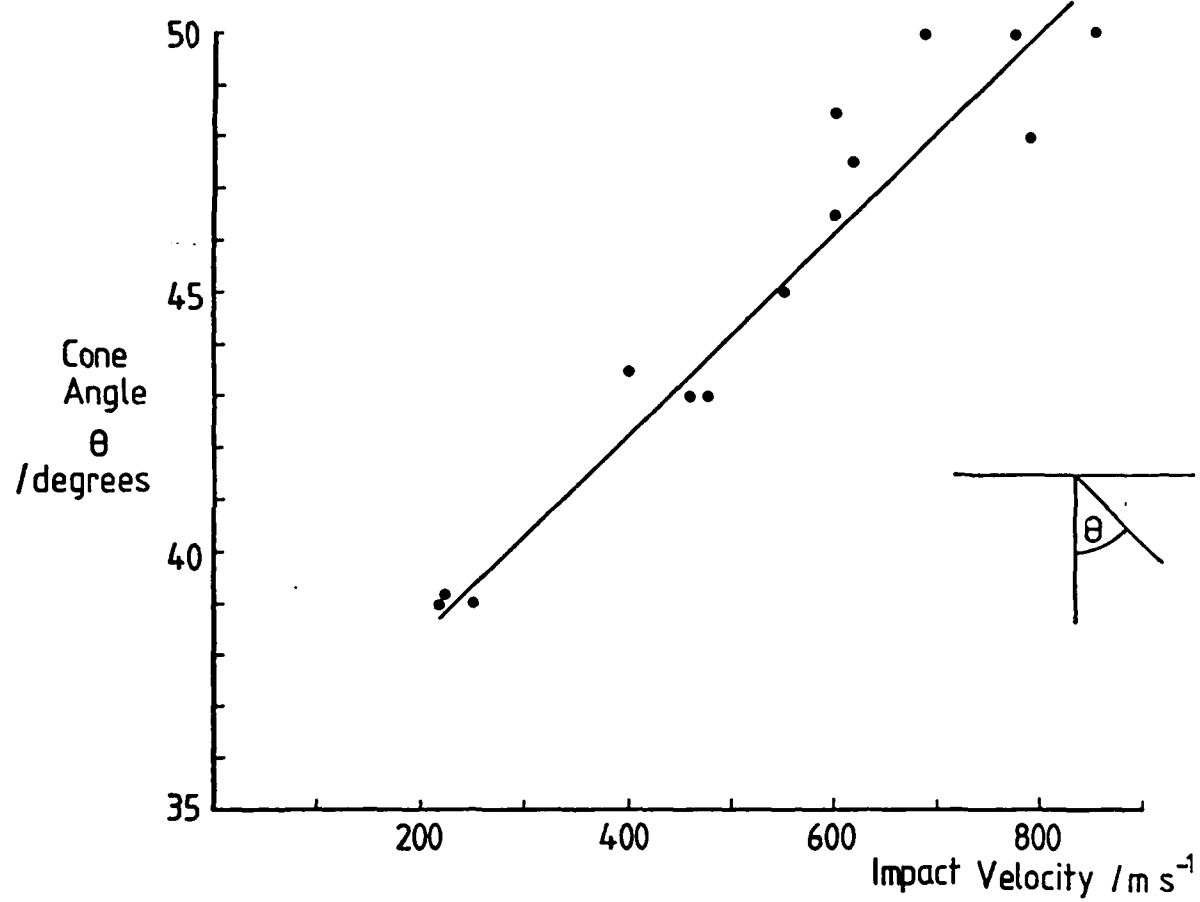


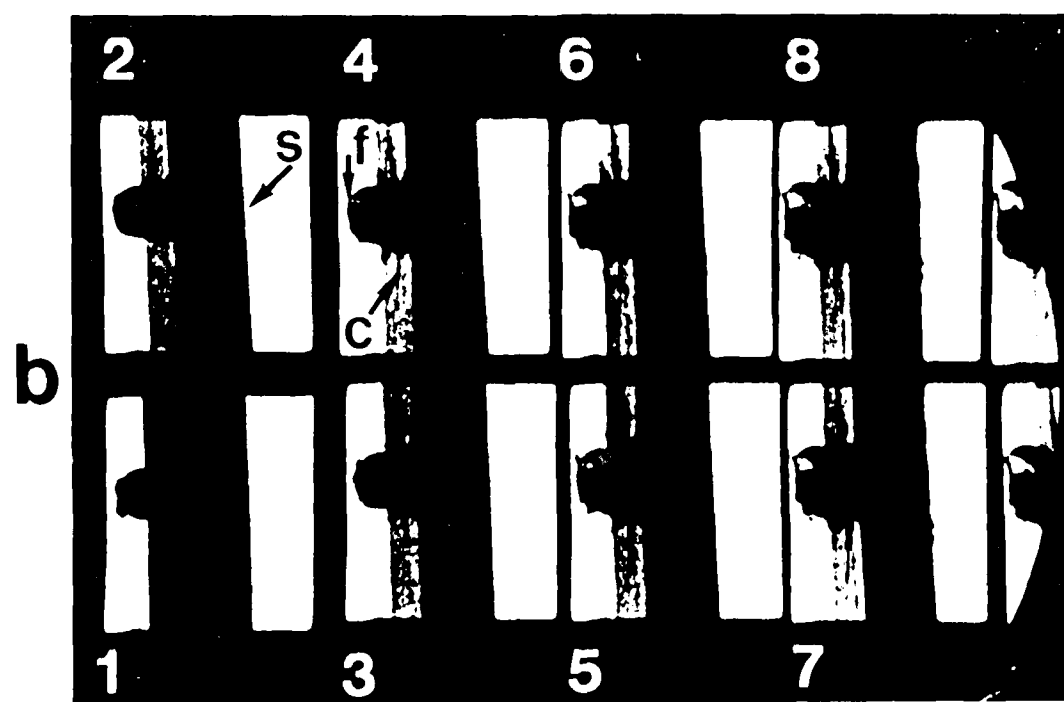
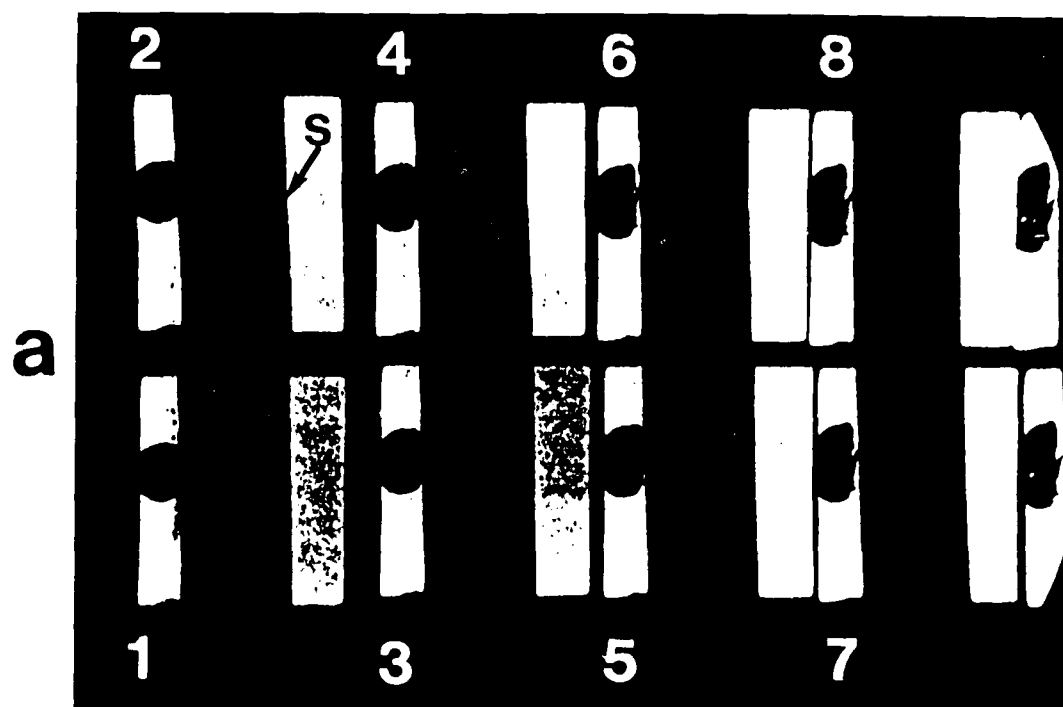
a)



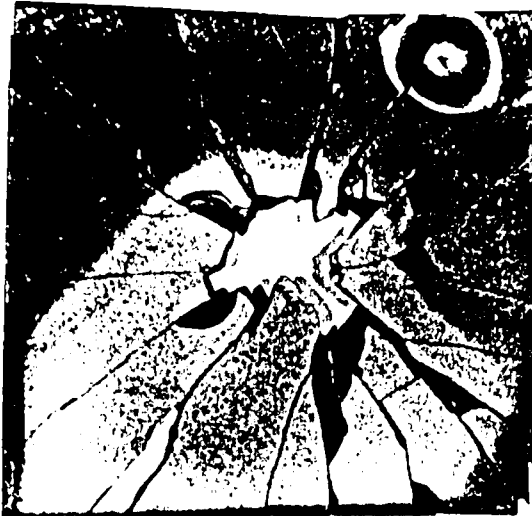
b)







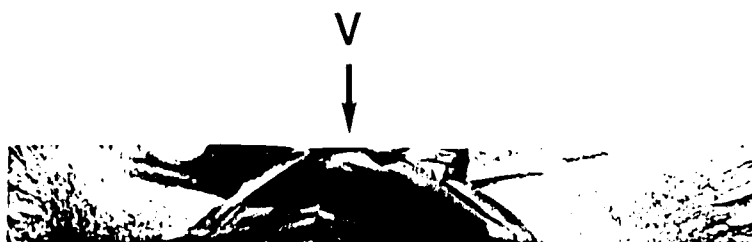
a



b



c



10mm,



END

4-87

DTIC